Spring 2020

Fundamental Studies of Bimetallic Model Surfaces and Metal Organic Framework Thin Films

Fathima Sharfa Farzandh

FUNDAMENTAL STUDIES OF BIMETALLIC MODEL SURFACES AND METAL ORGANIC FRAMEWORK THIN FILMS

by

Fathima Sharfa Farzandh

Bachelor of Science
University of Colombo, 2016

Submitted in Partial Fulfillment of the Requirements

For the Degree of Master of Science in

Chemistry

College of Arts and Sciences

University of South Carolina

2020

Accepted by:

Donna A. Chen, Director of Thesis

Michael L. Myrick, Reader

Cheryl L. Addy, Vice Provost and Dean of the Graduate School

DEDICATION

To my partner Grant Seuser for his endless support and encouragement throughout my graduate school career and my father for encouraging me to pursue higher education.

ACKNOWLEDGEMENTS

I would like to extend my gratitude to many people that helped me get through my master's program at the University of South Carolina. First of all, I would like to express my sincere appreciation to my advisor, Dr. Donna Chen, for her continuous motivation and guidance that helped me learn so much within a small time and become a better scientist. I would also like to thank Dr. Monnier from the department of chemical engineering for always sharing his wisdom about conventional catalysis and Dr. Myrick as well as the faculty and staff of the Department of Chemistry and Biochemistry for their help with everything. This journey would also be impossible without the help of former group members, Dr. Amy Brandt who trained me to take over the Leybold chamber with its magnificent capabilities to perform reactor studies. Dr. Grant Seuser, for his genius programming skills, insights into conventional catalysis synthesis and characterization methods as well as his endless companionship and Dr. Thathsara Maddumapatabandi for her help with gaining a basic understanding of working in a UHV lab. Additionally, I would like to thank the current group members, Dr. Gift Metavarayuth and Dr. Sumit Beniwal for sharing their postdoctoral wisdom from extended years of surface science research, Deepen for his insights with conventional reactor studies and reactor system maintenance and Narayan for his efforts to learn in a fast pace environment. I would also like to thank Dr. Karakalos Stavros for his invaluable help, kindness and insights on surface science techniques. Finally, I would like to thank all my amazing friends at the University of South Carolina, especially Moe Shonibare, for brightening up my time here.

ABSTRACT

This work is mainly focused on gaining a fundamental understanding of conventional bimetallic catalysts in order to correlate their macroscopic properties with the observed kinetic properties. This is achieved by synthesizing and studying fundamental model surface analogues of conventional catalysts that are difficult to study due to their complex, ill-defined nature. A wide array of surface science techniques that use ultra-high vacuum (UHV) conditions are readily available for detailed studies that can be conducted on model surfaces. This work focuses on the synthesis and investigation of two fundamental bimetallic catalysts formed via the addition of a second metal to an existing system in order to give rise to enhanced catalytic properties. The systems investigated are the bimetallic Pt-Sn catalysts and Cu-Rh metal organic frameworks consisting of benzene tricarboxylic acid (BTC) linkers.

Monometallic Pt catalysts with excellent hydrogenation properties can preferably undergo C=C hydrogenation and decarbonylation while the addition of oxophillic Sn to Pt to form bimetallic catalysts is reported to improve the selectivity to unsaturated alcohol synthesis via preferential C=O bond hydrogenation for larger aldehydes with substituted groups. The greater selectivity to unsaturated alcohol formation with the bimetallic Pt-Sn catalyst is claimed to stem from the presence of oxophillic Sn addition to Pt, which helps anchor the oxygen from the C=O bond due to electronic and/or geometric effects while Pt dissociates H_2 to synergistically hydrogenate the C=O bond. However, the exact source of the observed enhancement in selectivity is still unknown. Fundamental studies performed

using model Pt-Sn ordered alloys with different surface metal ratios show that the selectivity to furfural alcohol formation and the resistance to catalyst deactivation increases with the surface Sn concentration while there was observed to be an optimum Pt:Sn surface ratio at which there was maximum activity with 50% conversion. DFT calculations predict the formation of a η^1-(O)-intermediate that could be responsible for the observed selectivity to furfural alcohol formation.

The synthesis of thin MOF films is a rising area of interest due to its increasing applications and ability to function as a model system to study powder MOFs that also have high end applications. Using sophisticated surface science techniques such as X-ray photoelectron spectroscopy, grazing incidence wide angle X-ray scattering and atomic force microscopy, this work demonstrates that crystalline, monometallic Cu based BTC MOF films can be synthesized via layer-by layer dip coating method. Node metal replacement of this monometallic CuBTC with a second metal such as Rh is also shown to produce bimetallic CuRhBTC MOF thin films that play an important role in heterogeneous catalysis.

TABLE OF CONTENTS

DEDICATION……...iii

ACKNOWLEDGEMENTS……...iv

ABSTRACT……...v

LIST OF FIGURES……... x

LIST OF SYMBOLS……. xiv

LIST OF ABBREVIATIONS……xv

CHAPTER 1: INTRODUCTION……..1

1.1 HETEROGENEOUS MODEL CATALYSIS……1

1.2 BIMETALLIC CATALYSTS……2

1.3 MOTIVATION……2

1.4 REFERENCES……3

CHAPTER 2: EXPERIMENTAL……6

2.1 X-RAY PHOTOELECTRON SPECTROSCOPY (XPS)……... 6

2.2 UHV-COUPLED MICROREACTOR……7

2.3 SCANNING TUNNELING MICROSCOPY (STM)……..8

2.4 LOW ENERGY ION SCATTERING SPECTROSCOPY (LEIS)……..9

2.5 LOW ENERGY ELECTRON DIFFRACTION (LEED)……9

2.6 ATOMIC FORCE MICROSCOPY (AFM)……...…..10

2.7 GRAZING INCIDENCE WIDE ANGLE X-RAY SCATTERING (GIWAXS)…….11

2.8 REFERENCES…… 16

CHAPTER 3: THE FUNDAMENTALS OF SELECTIVE HYDROGENATION OF UNSATURATED ALDEHYDES WITH PT-SN BIMETALLIC CATALYST….. 17

3.1 INTRODUCTION……... 17

3.2 EXPERIMENTAL……...19

3.3 RESULTS…….24

3.4 DISCUSSION……..32

3.5 CONCLUSION…..……...37

3.6 ACKNOWLEDGEMENTS…….48

3.7 REFERENCES…… 48

CHAPTER 4: SYNTHESIS OF BIMETALLIC MOF THIN FILMS FOR FUNDAMENTAL STUDIES……... 55

4.1 INTRODUCTION……... 55

4.2 EXPERIMENTAL……...58

4.3 RESULTS AND DISCUSSION……..60

4.4 CONCLUSION……66

4.5 SUPPLEMENT INFORMATION SECTION……72

4.6 ACKNOWLEDGEMENTS……73

4.7 REFERENCES…… 73

LIST OF FIGURES

Figure 2.1: Setup used for XPS surface analysis 11

Figure 2.2: Schematic illustration of the reactor setup 12

Figure 2.3: The left image shows the outer appearance of the reactor (red box), feed manifold and the automatic sampling valves and the right image shows the inner reactor housing.. 12

Figure 2.4: Schematic illustration of the STM setup 13

Figure 2.5: Constant current and constant height STM imaging modes.....13

Figure 2.6: Summarized LEIS process 14

Figure 2.7: A typical LEED setup.....14

Figure 2.8: Schematic illustration of AFM imaging process.....15

Figure 2.9: Schematic illustration of GIWAXS scattering process 15

Figure 3.1: Furfural reaction scheme. (1) selective C=O hydrogenation; (2) decarbonylation; (3) nonselective decomposition, (4) ring hydrogenation, (5) ring opening reactions 39

Figure 3.2: Crotonaldehyde reaction scheme. (1) Selective C=O hydrogenation; (2) decarbonylation; (3) nonselective decomposition; (4) olefin bond hydrogenation; (5) secondary hydrogenation 39

Figure 3.3: Selectivity to furan as a funcntion of time for furfural reaction on different Pt(111) surfaces 40

Figure 3.4: Rate of furan formation as a function of time for for furfural reaction on different Pt(111) surfaces.....40

Figure 3.5: Selectivity to furfural alcohol as a function of time for furfural reaction on different Pt(111) surfaces.....41

Figure 3.6: Rate of furfural alcohol formation as a function of time for furfural reaction on different Pt(111) surfaces.....41

Figure 3.7: Non-selective decomposition as a function of time for furfural reaction on different Pt(111) surfaces.....42

Figure 3.8: Conversion % as a function of time for furfural reaction on different Pt(111) surfaces 42

Figure 3.9: THF selectivity % as a function of time for different Pt(111) surfaces 43

Figure 3.10: Butyraldehyde formation rate as a function of time for crotonaldehyde reaction on different Pt(111) surface 43

Figure 3.11: Conversion % as a function of time for crotonaldehyde reaction on different Pt(111)surfaces 43

Figure 3.12: Pt(4f) region for clean Pt(111) -red; 1ML Sn-Pt(111)-blue; 1ML Sn-Pt(111) 1000K alloy-green; 1ML Sn-Pt(111), 1000K post reaction-black 44

Figure 3.13: Sn(3d) region for clean Pt(111) -red; 1ML Sn-Pt(111)-blue; 1ML Sn-Pt(111) 1000K alloy-green; 1ML Sn-Pt(111), 1000K post reaction-black 44

Figure 3.14: post reactions O(1s) region for furfural hydrogenation reactions on 1ML Sn-Pt(111) 1000K alloy-red; 1ML Sn-Pt(111) 800K alloy-pink; Pt(111)-blue; crotonaldehyde hydrogenation reactions on 1ML Sn-Pt(111) 1000K alloy-green and Pt(111)-black.....45

Figure 3.15: post reactions C(1s) region for furfural hydrogenation reactions on 1ML Sn-Pt(111) 1000K alloy-red; 1ML Sn-Pt(111) 800K alloy-pink; Pt(111)-blue; crotonaldehyde hydrogenation reactions on 1ML Sn-Pt(111) 1000K alloy-green and Pt(111)-black.....45

Figure 3.16: STM images of 1ML Sn on Pt(111): a) after room temperature deposition; b)50 annealed to 800K for 1 minute; c) annealed to 1000K for 1 minute. All images are 110x110 $nm.^2$ 46

Figure 3.17: 1ML Sn-Pt(111) , 800 K alloy. Blue-($\sqrt{3}$ x $\sqrt{3}$) R30° Sn; Yellow-1x1) Pt ...46

Figure 3.18: 1ML Sn-Pt(111), 1000 K alloy. Blue-($\sqrt{3}$ x $\sqrt{3}$) R30° Sn; Red-p(2x2) Sn; Yellow-(1x1) Pt 46

Figure 3.19: Furfural binding configurations on Pt-Sn surfaces as a function of surface Sn coverage 47

Figure 3.20: Crotonaldehyde binding configurations on Pt-Sn surfaces as a function of surface Sn coverage 47

Figure 4.1: CuBTC synthesis and structure 67

Figure 4.2: Second metal incorporation via node metal exchange 68

Figure 4.3: Layer-by-layer growth of thin MOF films 68

Figure 4.4: Home-made automated dip coater used to soak the substrate in Cu acetate and H_3BTC solutions with ethanol rinsing steps in between to synthesize thin films of CuBTC 69

Figure 4.5: GIWAXS spectra for simulated CuBTC (a); Al_2O_3 -Si substrate (b); CuBTC thin film (c); $RhCl_3$ exchnaged CuBTC film (d); Rh acetate dip coated film(e) 69

Figure 4.6: XPS C(1s) spectra for films; $RhCl_3$ exchanged CuBTC (a); Rh acetate exchanged CuBTC (b); Rh acetate dip coated (c); $RhCl_3$ exchanged CuBTC with extended wash (d); CuBTC (e); Al_2O_3 -Si substrate (f) 70

Figure 4.7: Rh(3d) XPS region for as received Rh(III) chloride-red and Rh(II) acetate-blue standards also used as precursors for the Rh transmetallation 70

Figure 4.8: Rh(3d) XPS region for powder CuRhBTC MOF (a); $RhCl_3$ exchanged CuBTC film (b); Rh acetate exchanged CuBTC film(c); Rh acetate dip coated film(d); $RhCl_3$ exchanged film with extended wash (e) 70

Figure 4.9: Cl(2p) XPS reigion for films; $RhCl_3$ exchanged CuBTC (a); Rh acetate exchanged CuBTC (b); Rh acetate dip coated (c); $RhCl_3$ exchanged with extended wash (d) 70

Figure 4.10: Fitted Rh(3d) region for $RhCl_3$ exchanged film with extended wash showing the presence of Rh^{3+} and Rh^{2+} species 71

Figure 4.11: Cu(2p) XPS region for films; $RhCl_3$ exchanged CuBTC (a); Rh acetate exchanged CuBTC (b); Rh acetate dip coated(c); $RhCl_3$ exchanged with extended wash (d); CuBTC(e) 71

Figure 4.12: O(1s) XPS region for Al_2O_3 -Si substrate, CuBTC and Rh exchanged CuBTC films 71

Figure 4.13: CuBTC film grown from 40 cycles of dip coating. 5μm x 5μm 72

Figure 4.14: $RhCl_3$ exchanged CuBTC film. 5μm x 5μm 72

Figure 4.15: O(1s) XPS region for powder CuBTC and CuRhBTC MOFs plotted with that of as received Rh acetate.....72

LIST OF SYMBOLS

E_B	Binding energy
E_K	Kinetic energy
h	Plank's constant
ϕ	Work function
v	Frequency

LIST OF ABBREVIATIONS

AFM ..... Atomic force microscopy

BTC ..... Benzene tricarboxylic acid

DFT ..... Density functional theory

DMF ..... Dimethylformamide

FID ..... Flame ionization detector

GIWAXS ..... Grazing incidence wide angle X-ray scattering

LEED ..... Low energy electron diffraction

LEIS ..... Low energy ion scattering

ML ..... Monolayer

MOF ..... Metal organic framework

RMS ..... Root mean squared

STM ..... Scanning tunneling microscopy

THF ..... Tetrahydrofuran

TPD ..... Temperature programmed desorption

UHV ..... Ultra high vacuum

VASP ..... Vienna Ab initio simulation package

VLE ..... Vapor liquid evaporator

VT ..... Variable temperature

XPS ..... X-ray photoelectron spectroscopy

CHAPTER 1

INTRODUCTION

1.1 HETEROGENEOUS MODEL CATALYSIS

Heterogeneous catalysis is a form of catalysis where the catalyst is in a different physical phase than the reactants or products involved, the alternative being homogeneous catalysis. The origin of heterogeneous catalysis has brought about a major industrial breakthrough since it was first introduced over two centuries ago.[1–3] Its cost effective methods and sustainable industrial applications and processes permit engineering advantages that have led to covering almost 80% of the global market share with a constantly growing demand.[1,2] Among many industrial processes that dictate the economy, the current global production of ammonia, methanol, crude oil and fossil fuel all depend heavily on the development of highly efficient heterogeneous catalysts.[4] Hence, uncovering highly efficient and sustainable new avenues is key to overcoming the imminent energy and environmental challenges for a brighter tomorrow.

It is well known that heterogeneous catalytic reactions mostly occur on the low coordinated steps, edges and kink sites on the surface which are considered highly active sites.[5–9] However, there is very limited fundamental knowledge about the structure -activity correlation in commercial catalysts that are ill defined, highly complex material which makes them extremely complicated to study.[10,11] In order to deal with these complexities, model systems which can be single crystals, thin film or nano particles can be effectively employed. In simple terms, the said model systems can be considered fundamental 2D-

surface analogues of the complex commercial material which is in the form of a powder. Such model catalysts can be meticulously characterized in a pristine environment using a wide range of surface science techniques, under ultra-high vacuum (UHV) conditions (pressure ~$1x10^{-10}$ torr) unlike the high surface area commercial catalysts.[10,11]

1.2 BIMETALLIC CATALYSTS

In the context of synthesizing highly efficient catalyst, bimetallic catalysts play a pivotal role since they are commonly known for their synergistic properties that make them superior to their corresponding monometallic counterparts.[12,13] The enhancement in selectivity, activity and stability caused by the synergistic effects can be further categorized into electronic effects, geometric effects and bifunctional effects.[14–17] Both model systems studied in this work are bimetallic catalysts in which two metals play an active role to enhance the overall catalytic properties. Pt-Sn catalyst are known to display synergistic behavior due to the efficient hydrogenation properties of Pt combined with the oxophillic nature of Sn that will help anchor the C=O group in unsaturated aldehydes in order to promote preferential hydrogenation of C=O groups.[18,19] CuRhBTC MOF systems have Cu which provides structural integrity [20–22] to the MOF network while Rh provides sites for hydrogenation reactions.[23]

1.3 MOTIVATION

The synthesis and systematic characterization of fundamental surfaces warrant sophisticated surface science techniques for accurate correlations between macroscopic effects and kinetic processes. X-ray photo electron spectroscopy (XPS), scanning tunneling microscopy (STM), low energy electron diffraction (LEED), low energy ion scattering (LEIS), grazing incidence wide angle X-ray scattering (GIWAXS) and atomic force

microscopy (AFM) were few of the elaborate surface science techniques that were available at the University of South Carolina and used for this work. Regardless of vacuum studies being ideal for catalyst characterization itself, reactor studies performed under low pressures will reflect poorly on the true kinetics, due to being far from realistic pressure conditions under which commercial catalyst operate in industrial settings. By coupling a highly sensitive high-pressure cell suitable for reactor studies with model catalysts to an ultra-high vacuum (UHV) chamber that is capable of performing systematic surface science analysis, this pressure gap can be bridged.[24–26] This way, pre and post catalyst characterization can be conducted using sophisticated surface science techniques under UHV conditions, while accurate kinetic evaluations can be performed in the coupled microreactor, without exposure to air in between to procure the best of both worlds.

Well-ordered metal single crystals are commercially available to gain fundamental understanding of the real-world catalysts that are metals dispersed on high surface area supports. However, unlike metal single crystals, MOF thin films which are considered to be model systems of the 3D MOF networks are not highly available. Hence, developing methods to synthesize such thin film analogues have tremendous scope and utilization. Layer-by-layer growth method is an ideal technique to grow such thin MOF films and this work in combination with previous work[20] are the first instances of synthesizing bimetallic Cu based MOFs in the form of thin films to the best of our knowledge.

1.4 REFERENCES

1. Guo Y, Ren Z, Xiao W, Gao PX. Nano-Array Catalysts for Energy and Environmental Catalysis. In: *Catalysis by Materials with Well-Defined Structures*. Elsevier Inc.; 2015:339. doi:10.1016/B978-0-12-801217-8.00012-8
2. Unnikrishnan P, Srinivas D. Heterogeneous Catalysis. In: *Industrial Catalytic Processes for Fine and Specialty Chemicals*. Elsevier Inc.; 2016:41-111. doi:10.1016/B978-0-12-801457-8.00003-3

3. Baerns M. Aspects of Heterogeneous Catalysis and of Its Industrial and Environmental Practice. In: *Reference Module in Chemistry, Molecular Sciences and Chemical Engineering*. Elsevier; 2014. doi:10.1016/b978-0-12-409547-2.11041-8
4. Schlexer P. Computational Modeling in Heterogeneous Catalysis. In: *Reference Module in Chemistry, Molecular Sciences and Chemical Engineering*. Elsevier; 2017. doi:10.1016/b978-0-12-409547-2.14273-8
5. Lebedeva NP, Rodes A, Feliu JM, Koper MTM, Van Santen RA. Role of crystalline defects in electrocatalysis: CO adsorption and oxidation on stepped platinum electrodes as studied by in situ infrared spectroscopy. *J Phys Chem B*. 2002;106(38):9863-9872. doi:10.1021/jp0203806
6. Lebedeva NP, Koper MTM, Feliu JM, Van Santen RA. Role of crystalline defects in electrocatalysis: Mechanism and kinetics of CO adlayer oxidation on stepped platinum electrodes. *J Phys Chem B*. 2002;106(50):12938-12947. doi:10.1021/jp0204105
7. Birchem T, Pradier CM, Berthier Y, Cordier G. Hydrogenation of 3-methyl-crotonaldehyde on the Pt(553) stepped surface: Influence of the structure and of preadsorbed tin. *J Catal*. 1996;161(1):68-77. doi:10.1006/jcat.1996.0163
8. Yeates RC, Somorjai GA. The growth and alloy formation of copper on the platinum (111) and stepped (553) crystal surfaces; characterization by Leed, AES, and CO thermal desorption. *Surf Sci*. 1983;134(3):729-744. doi:10.1016/0039-6028(83)90070-5
9. Sheng T, Jiang YX, Tian N, Zhou ZY, Sun SG. *Nanocrystal Catalysts of High-Energy Surface and Activity*. Vol 177. 1st ed. Elsevier B.V.; 2017. doi:10.1016/B978-0-12-805090-3.00012-7
10. Motin AM, Haunold T, Bukhtiyarov A V., Bera A, Rameshan C, Rupprechter G. Surface science approach to Pt/carbon model catalysts: XPS, STM and microreactor studies. *Appl Surf Sci*. 2018;440:680-687. doi:10.1016/j.apsusc.2018.01.148
11. Freund HJ, Bäumer M, Libuda J, Risse T, Rupprechter G, Shaikhutdinov S. Preparation and characterization of model catalysts: From ultrahigh vacuum to in situ conditions at the atomic dimension. *J Catal*. 2003;216(1-2):223-235. doi:10.1016/S0021-9517(02)00073-8
12. Smith MW, Shekhawat D. Catalytic Partial Oxidation. In: *Fuel Cells: Technologies for Fuel Processing*. Elsevier; 2011:73-128. doi:10.1016/B978-0-444-53563-4.10005-7
13. Llorca J, Homs N, Sales J, Ramírez De La Piscina P. Support effect on the n-hexane dehydrogenation reaction over platinum-tin catalysts. *Stud Surf Sci Catal*. 1998;119:647-652. doi:10.1016/s0167-2991(98)80505-3
14. Dietrich PJ, Sollberger FG, Akatay MC, et al. Structural and catalytic differences in the effect of Co and Mo as promoters for Pt-based aqueous phase reforming catalysts. *Appl Catal B Environ*. 2014;156-157:236-248. doi:10.1016/j.apcatb.2014.03.016
15. Maris EP, Ketchie WC, Murayama M, Davis RJ. Glycerol hydrogenolysis on carbon-supported PtRu and AuRu bimetallic catalysts. *J Catal*. 2007;251(2):281-294. doi:10.1016/j.jcat.2007.08.007

16. Pagán-Torres YJ, Lu J, Nikolla E, Alba-Rubio AC. *Well-Defined Nanostructures for Catalysis by Atomic Layer Deposition*. Vol 177.; 2017. doi:10.1016/B978-0-12-805090-3.00017-6
17. Hakim SH, Sener C, Alba-Rubio AC, et al. Synthesis of supported bimetallic nanoparticles with controlled size and composition distributions for active site elucidation. *J Catal*. 2015;328:75-90. doi:10.1016/j.jcat.2014.12.015
18. Sankar M, Dimitratos N, Miedziak PJ, Wells PP, Kiely CJ, Hutchings GJ. Designing bimetallic catalysts for a green and sustainable future. *Chem Soc Rev*. 2012;41(24):8099-8139. doi:10.1039/c2cs35296f
19. Nakagawa Y, Tamura M, Tomishige K. Catalytic reduction of biomass-derived furanic compounds with hydrogen. *ACS Catal*. 2013;3(12):2655-2668. doi:10.1021/cs400616p
20. Brandt, A. J; Shakya D.M; Metavarayuth, K; Dolgopolova, E; Hensley, L; Duke, A.S; Farzandh, S; Shustova N. and DCA. Growth of Crystalline, Bimetallic Metal Organic Framework Films via Dip-Coating and Transmetallation. Manuscript in preperation.
21. Mazaj M, Čendak T, Buscarino G, Todaro M, Zabukovec Logar N. Confined crystallization of a HKUST-1 metal-organic framework within mesostructured silica with enhanced structural resistance towards water. *J Mater Chem A*. 2017;5(42):22305-22315. doi:10.1039/c7ta04959e
22. Szanyi J, Daturi M, Clet G, Baer DR, Peden CHF. Well-studied Cu-BTC still serves surprises: Evidence for facile Cu 2+/Cu + interchange. *Phys Chem Chem Phys*. 2012;14(13):4383-4390. doi:10.1039/c2cp23708c
23. Shakya DM, Ejegbavwo OA, Rajeshkumar T, et al. Selective Catalytic Chemistry at Rhodium(II) Nodes in Bimetallic Metal–Organic Frameworks. *Angew Chemie - Int Ed*. 2019;58(46):16533-16537. doi:10.1002/anie.201908761
24. Tenney SA, Xie K, Monnier JR, et al. Novel recirculating loop reactor for studies on model catalysts: CO oxidation on Pt/TiO2(110). *Rev Sci Instrum*. 2013;84(10). doi:10.1063/1.4824142
25. Yilmaz G, Peh SB, Zhao D, Ho GW. Atomic- and Molecular-Level Design of Functional Metal–Organic Frameworks (MOFs) and Derivatives for Energy and Environmental Applications. *Adv Sci*. 2019;6(21). doi:10.1002/advs.201901129
26. Fu Q, Wagner T, Rühle M. Hydroxylated α-Al2O3 (0 0 0 1) surfaces and metal/α-Al2O3 (0 0 0 1) interfaces. *Surf Sci*. 2006;600(21):4870-4877. doi:10.1016/j.susc.2006.08.008

CHAPTER 2

EXPERIMENTAL

2.1 X-RAY PHOTOELECTRON SPECTROSCOPY (XPS)

XPS is a UHV surface science analysis method that can provide qualitative and quantitative information about the elements (except H and He) present in a sample. Sophisticated applications of this technique can provide further information about the chemical environment, electronic structure and morphology of the surface.[1] The probe depth of X-rays can extend up to 10 nm, enabling analysis of the first few monolayers of a surface.[2] The underlying principles of XPS are the photoelectric effect and photo emission. X-ray irradiation can cause elements to emit photoelectrons from their core orbitals. These photoelectrons have characteristic binding energies, which enables elemental identification and quantitative analysis. The binding energy of the ejected photoelectrons relative to the fermi level, E_B, can be determined from the difference between the constant energy of the X-rays, hν, under vacuum, the kinetic energy E_K of electrons and the work function ϕ, which is the minimum energy required to remove an electron from the influence of the nucleus of an element. Equation 1 demonstrates this relationship.

$E_B = h\nu - E_K - \phi$ ---- **Equation 1**

Typical lab-based X-ray sources employ Mg or Al anodes for which, hν is 1253.6 eV and 1486.6 eV respectively. A series of electrostatic or magnetic lenses collects and focuses the photoelectrons into a hemispherical analyzer, which separates them based on

their kinetic energies before they are seen by the detector. The measured kinetic energies of the photo-ejected electrons are directly correlated to their binding energies, which are characteristic of the atoms from which they were emitted. Since core-level electrons do not participate in chemical bonding but are sensitive to changes in the electronic structure of the material, they provide elemental identification as well as information about the oxidation state of the surface components. Figure 2.1 illustrates the basic setup used for XPS analysis.

2.2 UHV-COUPLED MICROREACTOR

The custom built microreactor used for the reactor studies conducted with model Pt-Sn catalysts was coupled to the UHV chamber with two UHV proof valves positioned in-between the chamber and the reactor to withstand the pressure differential on the two sides.[3] This setup allowed samples to be well characterized with surface science techniques conducted under pristine UHV conditions while the kinetic evaluations were conducted under realistic pressure conditions for accurate correlation of macroscopic effects to the molecular level kinetics of the systems. In order to increase the sensitivity of the reactor to make it compatible with model catalysts that have far fewer active sites, it was made to have a small dead volume (18 cm^3) with the capacity to be used in recirculation mode where the reactants are sent past the catalyst multiple times to build sufficiently detectable concentration of products. However, due to the high activity of the Pt-Sn catalyst, the reactions were conducted in flow through mode with fresh reactant constantly passing through the catalyst. Figure 2.2 depicts a schematic of the microreactor discussed. The system is equipped with an automatic sampler that can sample a fixed volume (~1cm^3) of the reaction mixture at set intervals at which this small volume is sent to the GC (5890

series II) consisting of a fused silica capillary column (Rtx-5) with the dimensions 30 m length and 0.25 mm ID. At the end of the capillary column, the separated compounds will be burnt inside a flame ionization detector (FID) which will produce a signal proportional to the quantity of each compound eluted. This microreactor is capable of withstanding temperatures up to 190 °C and pressures near 1 atm. Figure 2.3 shows the outer view of the reactor system in the left image and the inner reactor housing in the right image.

2.3 SCANNING TUNNELING MICROSCOPY (STM)

STM is a type of scanning probe microscopy technique in which a sharp probe is scanned across the sample in a raster-fashion. This principle is used to map the morphology of the surface on the atomic scale.[1] STM employs the quantum tunneling of electrons, which can occur in vacuum when an atomically sharp tip is brought within a few angstroms of the surface of the sample with an applied voltage. Figure 2.4 illustrates the schematic view of an STM setup. STM can be conducted under constant current mode where the tunneling current is kept constant by maintaining a constant voltage in the piezoelectric element.[1] The voltage changes made to maintain the constant voltage will cause the piezoelectric crystal to move axially resulting in a mapped image of the surface which is the surface electron density as a function of vertical tip displacement. The tips can be made via electrochemical etching of a tungsten wire with a base like NaOH.[4] Once the tip is in the vacuum chamber it can be further conditioned by applying high voltage pulses to drive tungsten atoms to the apex of the tip to obtain atomic sharpness for undistorted STM images. In constant height mode the surface is scanned with the piezoelectric element maintained at a constant voltage to measure the tunneling current as a function of the position of the tip. Figure 2.5 illustrates the two typical STM imaging modes.

2.4 LOW ENERGY ION SCATTERING SPECTROSCOPY (LEIS)

LEIS also known as ion scattering spectroscopy (ISS) is a highly surface sensitive technique used to probe only the topmost atomic layer of a surface. The sample surface is bombarded with low energy ions of an inert gas, typically He^+, Ne^+ or Ar^+, and an electrostatic analyzer is used to determine the kinetic energy of the ions that survive backscattering from different elements on the surface. Figure 2.6 illustrates the summarized process of the LEIS technique. Since only the ions backscattered from the topmost layer will have sufficient energy to reach the detector, this technique enables the determination of the surface composition of only the first monolayer. Elemental identification is possible because the mass of the surface atom that caused the backscattering event to occur can be back calculated using the kinetic energy of the scattered ions based on the principles of conservation of momentum, considering it to be a two-body elastic collision.

2.5 LOW ENERGY ELECTRON DIFFRACTION (LEED)

In the late 1920s it was discovered that electrons can also be diffracted by crystalline solids, similar to X-rays. Thereby began the use of LEED for crystal structure determination of single crystals, ordered overlayers of thin films or adsorbates. A typical LEED setup is displayed in Figure 2.7. Here, an electron beam with variable energy is produced by an electron gun and directed on the sample surface. The electrons then backscatter from the sample surface onto a series of grids surrounding the electron gun. The backscattered electrons can be elastically scattered electrons that forms a set of diffracted beams which form the LEED pattern or the less significant inelastically scattered electrons which can consist of up to 99% of the total flux. These inelastically scattered electrons are filtered out while the elastically scattered fraction is accelerated towards a

phosphorous screen. These electrons coming in to contact with the phosphorous screen will create a diffraction pattern of bright green spots corresponding to the periodicity of the surface probed from the constructive interference of electron waves. A LEED pattern represents reciprocal space, meaning that the distances between the bright spots in the LEED pattern are inversely proportional to the distance between the points in the actual surface.

2.6 ATOMIC FORCE MICROSCOPY (AFM)

AFM is a scanning probe microscopy method in which a probe/cantilever that has a sharp, force sensing tip that is allowed to interact with the sample surface is placed parallel to the surface. With the change in the interaction force between the cantilever tip and the surface, deflections are produced in the cantilever.[1] These deflections are measured to be used to construct a topographic image of the surface that will enable determination of the dimensions of the features observed on a surface.[1] This process is schematically illustrated in Figure 2.8. Existing microscopes can image surfaces based on the principles of a wide range of forces including electrostatic and magnetic forces. Because AFM is based on a force measurement there is no restriction requiring the sample to be an electrical conductor unlike with STM. When AFM is used in the non-contact (tapping) mode, the cantilever oscillates at a fixed resonance frequency. However, when the tip comes close to a surface feature, forces from the feature can interact with the cantilever to decrease its resonance frequency. In order to maintain the initial resonance frequency, the distance between the tip and sample must be adjusted. The height adjustments made in such way is used to map the topography of the surface.[5]

2.7 GRAZING INCIDENCE WIDE ANGLE X-RAY SCATTERING (GIWAXS)

GIWAXS is a method to analyze crystal structure in the nanoscale by measuring the intensity of the scattered X-rays as a function of angle. Structural information can be collected in the transmission or grazing incidence mode to deduce structure of a wide range of materials.[6] In the experimental process used to analyze thin MOF films, X-rays were directed to the surface to be analyzed at a grazing incidence angle to increase signal sensitivity and to account for the non-transparent nature of the substrates. The angle of incidence can be adjusted to probe only the topmost layer up to a depth of 10 nm or deeper for thicker samples. The scattered X-rays are identified by a 2D area detector which is schematically illustrated in Figure 2.9. The 2D area detector image can be reduced to a 1D intensity vs momentum transfer (I vs q) curve in which the slope of the curve and/or the oscillations within it contains structural information. When the 2D detector is placed at a wide angle, information about crystal structure can be obtained.[7]

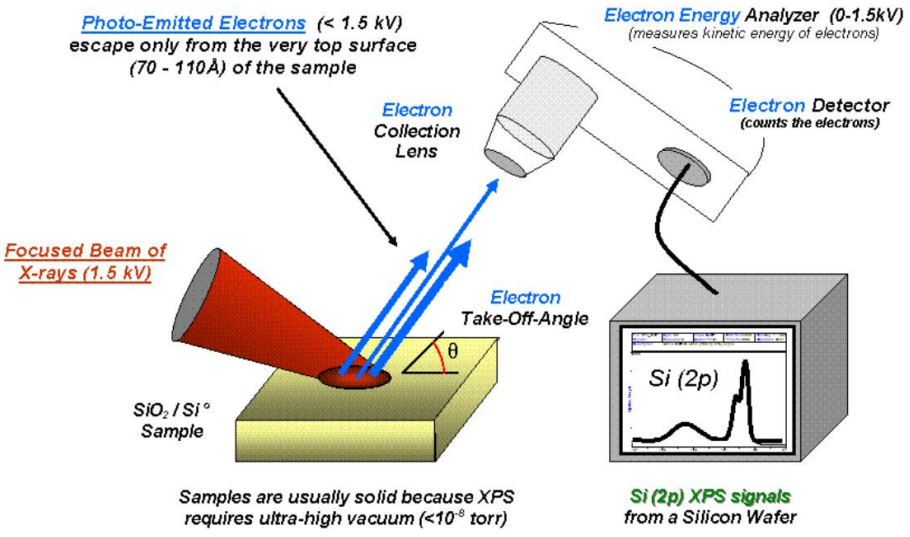

Figure 2.1: Setup used for XPS surface analysis[8]

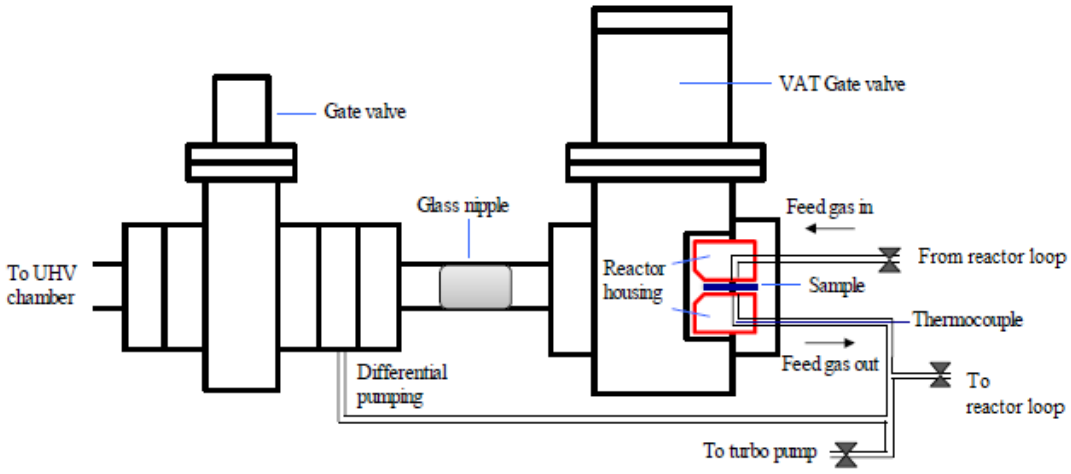

Figure 2.2: Schematic illustration of the reactor setup[3]

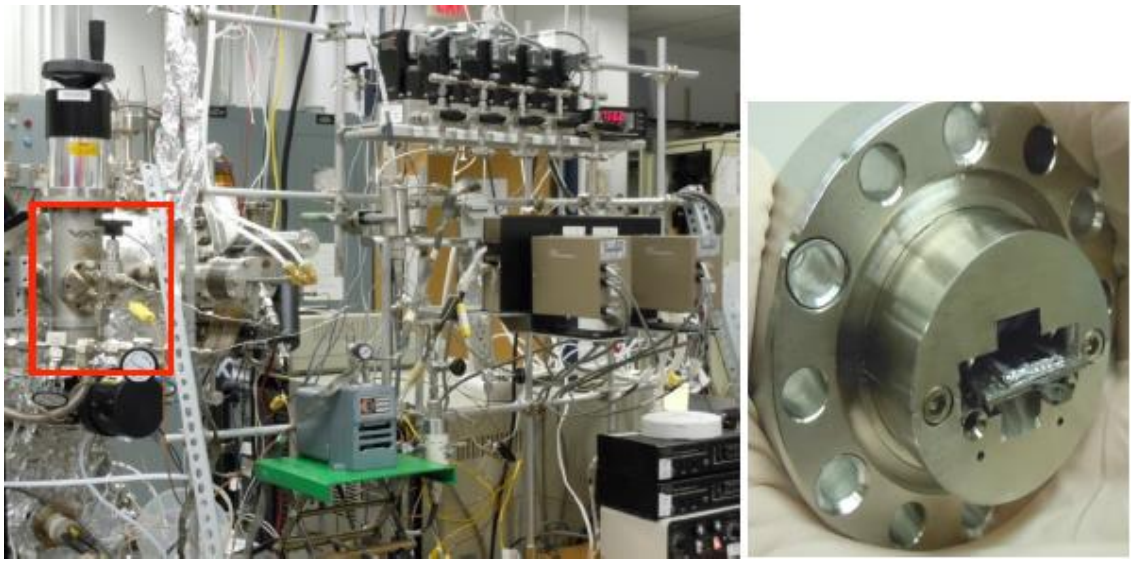

Figure 2.3: The left image shows the outer appearance of the reactor (red box), feed manifold and the automatic sampling valves and the right image shows the inner reactor housing[3]

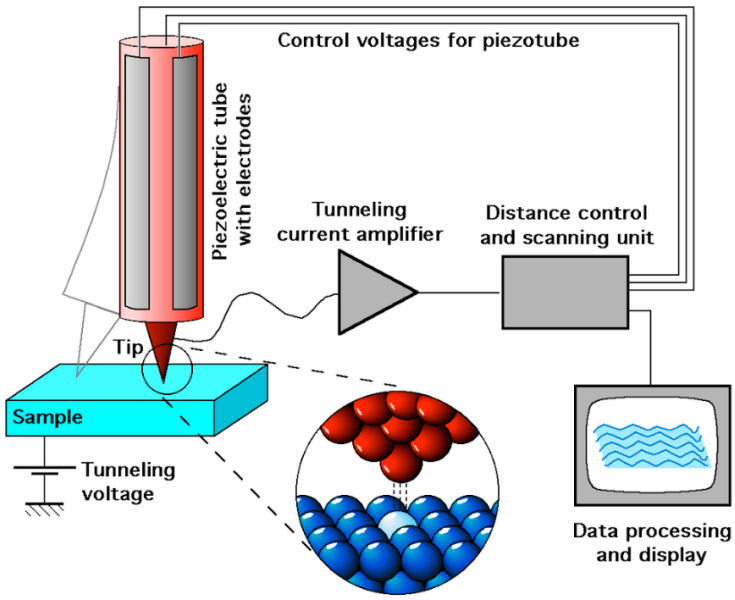

Figure 2.4: Schematic illustration of the STM setup[9]

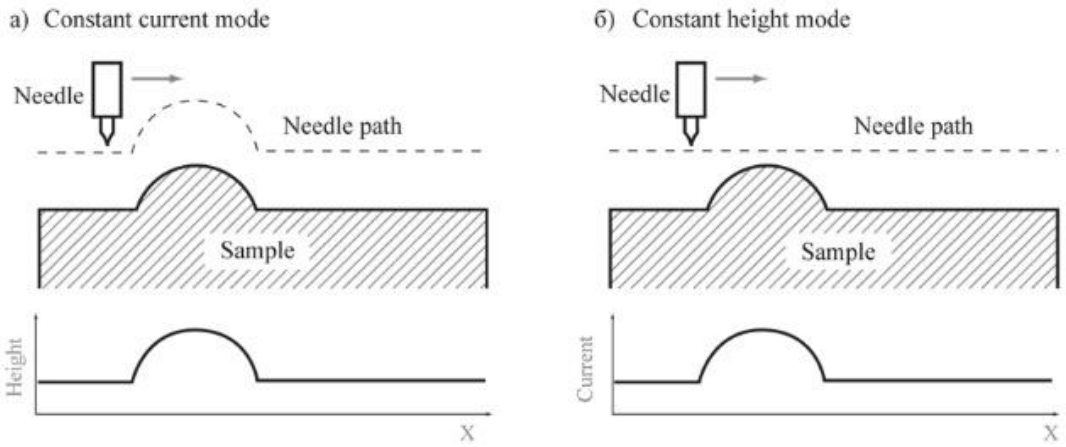

Figure 2.5: Constant current and constant height STM imaging modes[10]

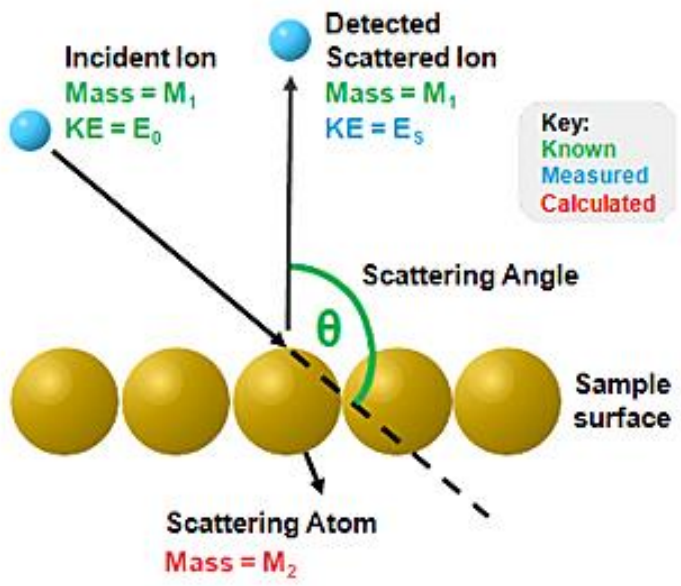

Figure 2.6: Summarized LEIS process[11]

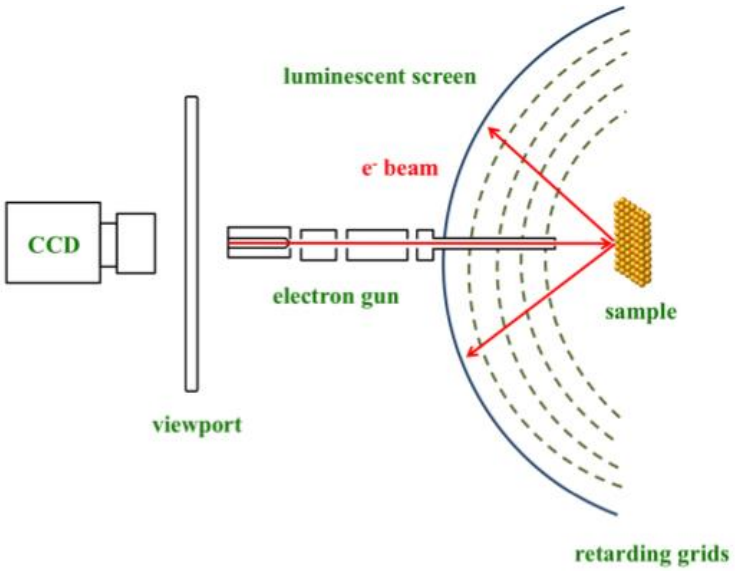

Figure 2.7: A typical LEED setup [12]

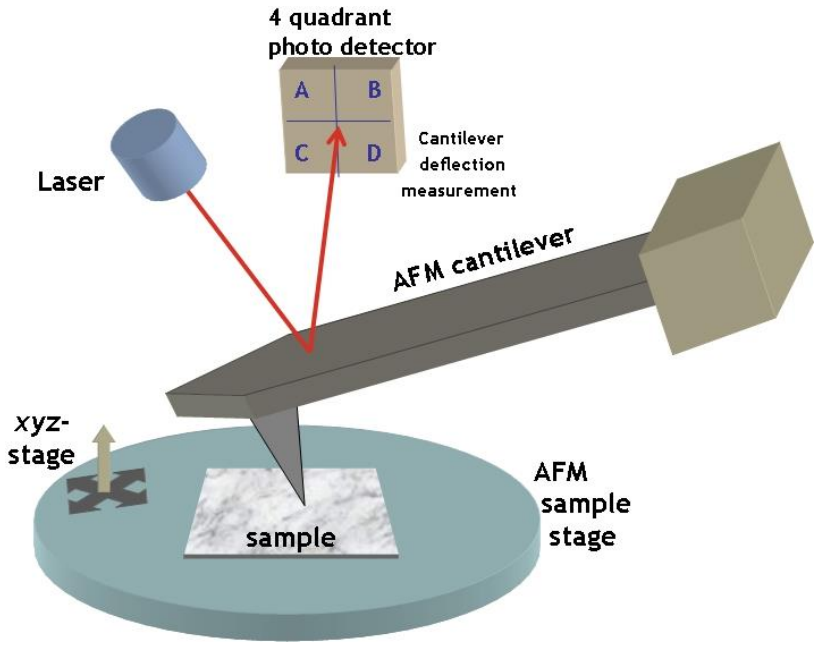

Figure 2.8: Schematic illustration of AFM imaging process[13]

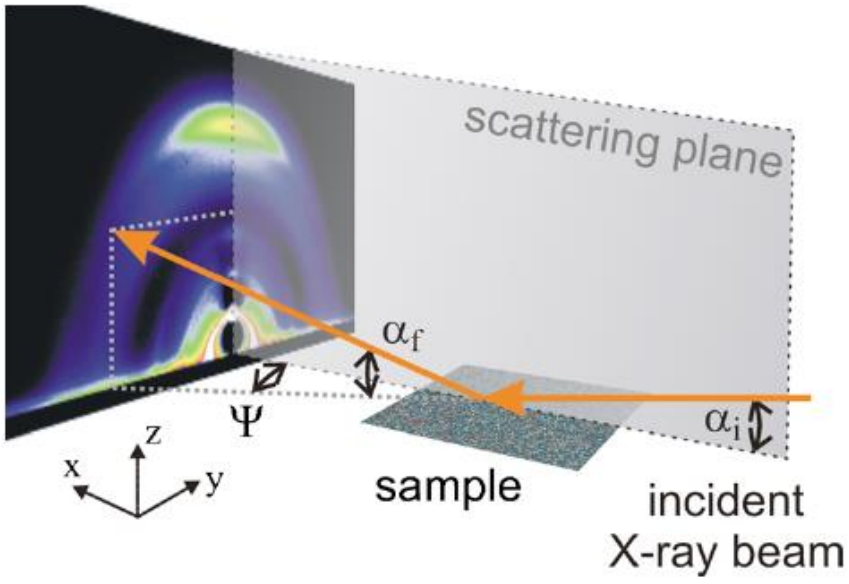

Figure 2.9: Schematic illustration of GIWAXS scattering process[7]

2.8 REFERENCES

1. Vickerman JC, Gilmore IS. *Surface Analysis - The Principal Techniques: Second Edition*. (Vickerman JC, Gilmore IS, eds.). Chichester, UK: John Wiley and Sons; 2009. doi:10.1002/9780470721582
2. Carvalho LC. X-ray photoelectron spectroscopy. http://doi.wiley.com/10.1002/9780470721582. Published March . Accessed March 3, 2020.
3. Tenney SA, Xie K, Monnier JR, et al. Novel recirculating loop reactor for studies on model catalysts: CO oxidation on Pt/TiO2(110). *Rev Sci Instrum*. 2013;84(10). doi:10.1063/1.4824142
4. Park JB, Conner SF, Chen DA. Bimetallic Pt - Au Clusters on TiO 2 (110): Growth , Surface Composition , and Metal - Support Interactions. 2008;2(110):5490-5500. doi:10.1021/jp076027n
5. Gross L, Mohn F, Moll N, Liljeroth P, Meyer G. The chemical structure of a molecule resolved by atomic force microscopy. *Science (80-).* 2009;325(5944):1110-1114. doi:10.1126/science.1176210
6. Feigin LA, Svergun DI. *Structure Analysis by Small-Angle X-Ray and Neutron Scattering*.; 1987. doi:10.1007/978-1-4757-6624-0
7. Perlich J, Rubeck J, Botta S, et al. Grazing incidence wide angle x-ray scattering at the wiggler beamline BW4 of HASYLAB. *Rev Sci Instrum*. 2010;81(10). doi:10.1063/1.3488459
8. X-ray photoelectron spectroscopy. https://en.wikipedia.org/wiki/X-ray_photoelectron_spectroscopy (accessed Mar 4, 2020).
9. Scanning Tunneling Microscopy https://commons.wikimedia.org/w/index.php?curid=180388 (accessed Mar 4, 2020.
10. STM operation modes. http://eng.thesaurus.rusnano.com/wiki/article14154. Accessed March 4, 2020.
11. Ion Scattering Spectroscopy https://xpssimplified.com/ion_scattering_spectroscopy.php (accessed Mar 4, 2020).
12. Low energy electron diffraction By OpenStax (Page 3/5) | Jobilize LLC https://www.jobilize.com/physics4/course/7-2-low-energy-electron-diffraction-by-openstax?page=2 (accessed Mar 4, 2020).
13. Atomic force microscopy https://simple.wikipedia.org/wiki/Atomic_force_microscope (accessed Mar 4 2020)

CHAPTER 3

THE FUNDAMANTALS OF SELECTIVE HYDROGENATION OF UNSATURATED ALDEHYDES WITH PT-SN BIMETALLIC CATALYSTS

3.1 INTRODUCTION

Selective hydrogenation of unsaturated aldehydes to produce their corresponding unsaturated alcohol is a key reaction in the production of several value-added chemicals with extensive industrial applications. In general, they are used to manufacture perfumes, flavorings and pharmaceuticals among others.[1–5] Furfural/furfuryl alcohol and crotyl alcohol are two such unsaturated alcohols among the most important of these value added chemicals with additional applications in the manufacturing of lubricants, lysine, vitamin C and dispersing agents for the former.[6–9] However, the selective hydrogenation to produce unsaturated alcohol is complicated by the competitive olefinic, C=C bond hydrogenation which is thermodynamically and kinetically preferable under most conditions.[10–12] The C=C bond hydrogenation is thermodynamically favored by approximately 35 kJ/mol, compared to C=O bond hydrogenation.[13] Due to the multiple functional groups available in unsaturated aldehydes such as furfural and crotonaldehyde, there can be multiple undesirable reaction pathways such as decarbonylation, non-selective decomposition, ring hydrogenation and ring opening reactions[14–17] as depicted in Figure 3.1. With crotonaldehyde there are fewer types of undesirable reactions that can occur since it is a

less complex molecule. As seen in Figure 3.2, olefinic C=C bond hydrogenation, decarbonylation, non-selective decomposition and secondary hydrogenation to make the saturated alcohol are among these.

Combining a noble metal with good hydrogenation properties (ex: Pt, Pd) with a second oxophillic metal that would help anchor the C=O bond (ex: Re, Sn, Fe, Zn) is a common strategy used in the development of catalysts that are active and selective for C=O bond hydrogenation.[18–20] Supported Pt-Sn bimetallic catalysts that fall in to this category are recognized for their suitability to be used in hydrocarbon conversion reactions and have been used for hydrogenation-dehydration,[21] selective oxidation[22] and hydrogenolysis[23] reactions. The synergistic behavior of bimetallic Pt-Sn compared to monometallic Pt catalyst gives rise to different catalytic activity and greater stability from resistance to coke formation.[24–26] The conversion of unsaturated aldehydes to their corresponding alcohols via selective hydrogenation is amongst the reactions that give promising results with Pt-Sn bimetallic catalyst.[5] The enhanced selectivity obtained from Pt-Sn catalyst is broadly attributed to two main effects. The formation of bimetallic alloys,[1,5,21] or that of Sn oxide.[10,27,28] Alloy formation is further categorized to occur from the dilution of Pt ensemble to reduce C=C bond hydrogenation, C-C and C=O bond scission[21,27,29–31] and/or electronic effects.[32–34] However, there is still a lack of fundamental understanding about the exact nature of the synergistic behavior of the bimetallic Pt-Sn catalysts for selective hydrogenation reactions.[5,35]

Supported Sn-Pt catalysts are high surface area catalysts with a complex structure which will make structure-kinetic correlations more complicated. Sn-Pt alloys made on Pt(111) on the other hand helps factor out many such undesirable support effects prevalent

in the supported catalysts in order to simplify the system. Metal-support interaction, incomplete reduction of metals, particle size effects and sintering are among the factors that can be taken out of the picture for fundamental studies.[5,36] Hence, this study investigates the fundamental effects of alloy formation on the selective hydrogenation of unsaturated aldehydes by systematically probing the monometallic and bimetallic Pt-Sn alloy compositions on well-defined model catalysts to methodically study their selectivity and activity as a function of the catalysts' structural aspects.

3.2 EXPERIMENTAL

Catalyst preparation and characterization were performed in two ultra-high vacuum (UHV) chambers that have been described in detail elsewhere. The first chamber [37,38] has a base pressure $<5x10^{-10}$ torr. Among other instrumentation, this chamber is equipped with a four-pocket electron-beam evaporator (Oxford Applied Research, EGCO4) for metal deposition which was used to make the Pt-Sn bimetallic surfaces. Additionally, it also includes a hemispherical analyzer SPHERA II integrated with Mg/Al Kα X-ray sources (Omicron, DAR 400) operated at 15 kV and 20 mA emission current for X-ray photoelectron spectroscopy (XPS) analysis. Catalyst were prepared for the reactor studies in the first chamber that is coupled to a custom built microreactor in such a manner that it can be completely isolated from the chamber except during sample transfer.[39]

The second chamber [40,41] that has a base pressure $<2x10^{-10}$ torr is equipped with a variable-temperature scanning tunneling microscope (Omicron, VT-STM) a hemispherical analyzer (Omicron EA125) for XPS and low energy ion scattering spectroscopy (LEIS), as well as optics for low energy electron diffraction (LEED) analysis.

Catalyst preparation

Monometallic and bimetallic catalysts were prepared using a Pt(111) single crystal (99.999%, Princeton Scientific Corp., 8 mm diameter, 2 mm thickness) mounted on a standard Ta Omicron sample holder plate in to which a 8.9x8.9 mm^2 window was cut, while two Ta wires are spot welded on it to seat the crystal in place by press-fitting the Ta wires in 1.1mm deep slots cut in to its sides. This Pt(111) crystal was cleaned using Ar^+ ion sputtering at 1 kV and 10 mA for 20 minute followed by an annealing step where the crystal was heated to 950 K for 1 minute with the sample directly heated through the window in the sample plate, using a Tungsten filament via electron beam heating. The sample annealing temperature and the rate of heating/cooling step which was maintained at 2 K/s was monitored using an infrared pyrometer (HEITRONICS, D65205 Wiesbaden). Bimetallic Pt-Sn surfaces were made via the evaporation of Sn using pellets (ESPI, 5N purity, 1-3 mm) placed in a Ta crucible. Sn coverages of 0.5 monolayer (ML) and 1ML were deposited on Pt(111) where a monolayers is defined relative to the surface packing density of Pt(111) (1 ML = 1.5x 10^{15} atom/cm^2). Sn was deposited on Pt(111) via physical vapor deposition method, at a rate of ~0.05 ML/min, measured using an independently calibrated quartz crystal microbalance flux monitor (QCM, Inficon, XTM-2). Pt-Sn ordered alloys were synthesized by annealing the surface to a given temperature (800-1000 K) following the initial Sn deposition which was a procedure borrowed from the literature.[5,42]

Reactor studies

Samples prepared in the UHV chamber were directly transferred in to the coupled microreactor via linear transfer enabled by a transfer arm, without the sample being

exposed to air or breaking vacuum. H_2, which also acted as the sweep gas for the reaction was introduced via an independently calibrated mass flow controller (Brooks, 5890i) that was directed to a homemade stainless-steel vapor liquid equilibrator (VLE) containing a liquid chemical at a time, to obtain the low concentrations of vapor phase unsaturated aldehyde in balance H_2.

The temperature of the sample was monitored with a type K thermocouple (Omega, KMQSS-040G-6) welded into the feed gas inlet, beside the surface of the sample. The gas lines were maintained at ~80 °C to avoid condensation of unsaturated aldehydes in the lines, using two Valco Instruments temperature controllers. Pressure was monitored by two capacitance manometers (MKS Instruments, Baratron 722A) located upstream of the reactor in the feed gas line (790 Torr ~ 800 Torr) and downstream of the reactor (770 Torr ~ 780 Torr). Dilute feed concentrations of the unsaturated alcohols were used in the reactor studies to avoid polymerization[9,15,43] in the gaslines while the low total feed gas flows 20-25 sccm would maximize the feed contact time in order to increase conversion. The reaction temperatures, 160 ºC and 80 ºC were chosen because maximum selectivity to the unsaturated alcohol formation is reported at these temperatures.[5,17,44,45]

The catalytic conversions and product distribution for monometallic Pt(111) as well as three Pt-Sn ordered alloys with different surface compositions were investigated in the UHV coupled microreactor for furfural hydrogenation reactions. The reaction was conducted in the microreactor used in the flow reactor mode with 0.1% furfural (Sigma Aldrich, 99%) balance H_2 (Airgas, 99.999%) at 1 atm pressure and a total feed gas flow of 20 sccm (measured using a digital flow meter (Agilent Technologies, ADM2000)) at 160 ºC temperature. The product distributions, selectivity and conversions for monometallic

Pt(111) as well as a Pt-Sn alloy mixture of ordered p2x2 and √3x√3 R30º structures were also studied for crotonaldeyhe hydrogenation reactions. The reaction was conducted using 0.27% crotonaldehyde balance H_2 with a total feed gas flow of 25 sccm at 80 ºC temperature and 1 atm pressure. For both the reactions studied, once the feed mixture was introduced to the catalyst, a volume of ~1.096 cm^3 from the reaction mixture was sampled with a 1:10 split ratio, every 30 minutes, using an automatic sampling system to analyze the product distribution with a gas chromatograph (HP 5890 series II). This GC was integrated with a Rtx-5 capillary column (0.25 mm ID, 30 m length, RESTEK) that carries the separated components to a flame ionization detector (FID). The column was maintained at 50 ºC and 40 ºC under isothermal conditions for furfural and crotonaldehyde reactions respectively in order to obtain the maximum separation between the aldehyde and the corresponding unsaturated alcohol. Background subtractions were carried out to correct for the formation of certain products via unsaturated aldehyde decomposition on the stainless-steel reactor walls/lines. Reactant and product calibrations were performed by headspace sampling of furfural alcohol (Sigma Aldrich, 98%), furan (Sigma Aldrich, >99%), tetrahydrofuran/THF (Sigma Aldrich, >99.0%), butyraldehyde (Sigma Aldrich, >99.0%) and crotyl alcohol (Sigma Aldrich, 96%) to calculate FID response factors for rate calculations. The conversion at a given time was calculated using the quantity of reactant unsaturated aldehyde as seen in the equation below.

$$\text{Conversion} = \frac{\text{Reactant in the feed(nmol)} - \text{Reactant at a given time(nmol)}}{\text{Reactant in the feed(nmol)}} \%$$

The selectivity towards a specific product at a given time was calculated using the equation given below,

$$\text{Selectivity} = \frac{\text{Rate of formation for a given product at a given time (nmol)}}{\text{Rate of total prodcut formation at the given time (nmol)}}\%$$

The non-selective decomposition % was calculated using a difference measurement by subtracting furfural alcohol, furan and THF selectivities from a unity by assuming that all furfural that did not get converted to either furfural alcohol, furan or THF underwent decomposition and that these were the only possible reaction pathways since these were the only pathways for which products were observed.

$$\text{Non selective decomposition } \% = 1 - (\text{furfural alcohol} + \text{furan} + \text{THF selectivity})\%$$

Catalyst characterization

For qualitative as well as quantitative elemental analysis, XPS was performed in the first chamber coupled to the reactor, using the Mg Kα X-ray source. The Pt(4f), Sn(3d), C(1s) and O(1s) regions were scanned with a 0.2 s dwell time and a 0.025 eV step size for monometallic Pt and the PtSn surfaces prepared using the Pt(111) single crystal. The binding energies of Pt(4f) and Sn(3d) pre and post reaction enabled understanding what occurred to the catalyst under reaction conditions. The low-resolution survey region was scanned with a 0.2 s dwell time and a 0.5 eV step size to verify that there was no contamination problem introduced in the sample preparation step as well as during reaction.

Scanning tunneling microscopy (STM) and LEED experiments were carried out in the second chamber. The STM studies were conducted with an Omicron VT-STM to investigate the growth and surface morphology of Pt and Sn clusters as well as alloy formation on Pt(111). STM images were collected at 0.1-0.2 nA constant tunneling current for Pt(111). STM tips were made by electrochemically etching a 0.38 mm diameter tungsten wire in NaOH.[46] Tips were further conditioned by sputtering with argon ions at 3

kV and pulsing at higher voltages up to 10 V. LEIS experiments were conducted using He^+ ions with a low energy of 600 eV and the acquisition times were adjusted to minimize sample destruction during data collections. LEED analysis was performed using 80 eV beam energy.

DFT calculations

Density functional theory (DFT) calculations were conducted by the Henkelman group from the University of Texas, Austin, using the Vienna Ab-Initio Package.[47,48] Core electrons were described within the projected augmented wave framework;[49] valence electrons were described with a plane wave basis set up. The generalized gradient approximation in the form of the Perdew, Burke and Ernzerhof functional was utilized to model electronic exchange and correlation.[50] The Brillouin zone was sampled using Monkhorst pack with a K-point density of 2 2 1. This is found to be adequate for binding energy calculations for the surfaces introduced in this chapter. The Pt(111) slab contains 16 atoms in each layer and a total of 4 layers, with the bottom two layers constrained to their positions in bulk while the top two layers are allowed to relax. Pt_3Sn (p2x2), Pt_2Sn ($\sqrt{3}x\sqrt{3}$ R30º) and PtSn slabs with Sn compositions of 25%, 33% and 50% respectively were simulated using VASP code and PBE-GGA exchange correlation functional with an energy cutoff of 400 eV to calculate upright and flat binding energies of unsaturated aldehydes on these surfaces.

3.3 RESULTS

This study was carried out in order to obtain fundamental insights into the gas phase selective hydrogenation reactions of unsaturated aldehydes, using monometallic Pt as well as bimetallic Pt-Sn alloy catalysts. Two unsaturated aldehydes, furfural and crotonaldehyde

were used for the synthesis of their corresponding unsaturated alcohol which has important applications in industry.[5,9,51–53] The said reactor studies were performed with model monometallic Pt(111) and Pt-Sn bimetallic ordered alloys as a comparative study to investigate the source of the selectivity enhancement to furfuryl alcohol formation with bimetallic catalysts and identify the optimum bimetallic compositions that will preferably synthesize the unsaturated alcohol in good yield.

Selective hydrogenation of furfural

Furfural hydrogenation reaction studies conducted with monometallic Pt(111) surface displayed the highest selectivity to decarbonylation and formed furan as the major product as illustrated in Figure 3.3-3.4, agreeing with other reports from the literature.[14,51,54] The furan rate of formation was highest for this surface, although it dropped off rapidly, indicating prompt catalyst deactivation. No furfural alcohol was detected on Pt(111) which is again in agreement with the literature.[14,51] Ring hydrogenation and ring opening products such as THF, butanol and C_3-C_4 hydrocarbons were detected in small amounts from the reaction on this surface. This surface also demonstrated a low conversion of only 10%. The three ordered Pt-Sn bimetallic alloys that were used for reactor studies only produced furfural alcohol, furan and THF. The alloy surfaces used were 1 ML Sn deposited on Pt(111) annealed to 800 K for 1 minute, 1 ML Sn deposited on Pt(111) annealed to 1000 K for 1 minute and 0.5 ML Sn deposited on Pt(111) annealed to 1000 K for 1 minute. Out of these surfaces, the first two demonstrated stable selectivity for furfural alcohol formation (see Figure 3.5 showing selectivities settle at 70% and 60% with greater selectivity observed when annealed to a lower temperature). However, as shown in Figure 3.6, the rate of formation of furfural alcohol was > 4 times higher with no

loss of activity for over 6 hours with the 1000 K annealed surface (~17 μmol/hr), corresponding to a 50% conversion. Compared to this, the 800 K annealed alloy for which the rate of furfural alcohol formation started off at ~11 μmol/hr, dropped to ~4 μmol/hr corresponding to a decreasing conversion that finally settled at only ~10% by the end of 6 hours. Furthermore, the furan and THF selectivities were near 2% each for both of the 1 ML Sn on Pt(111) alloys. Leading to non-selective decompositions near ~33% and ~26% for the 1000 K alloy and 800 K alloy respectively (Figure 3.7). Selectivity, conversion and rate values are averaged over the last 4 hours when they seemed to settle unless mentioned otherwise. Hence, selectivities for furfural alcohol formation, decarbonylation and non-selective decomposition observed between the two 1ML Sn-Pt alloys indicate similar trends. However, the 1000 K alloy had >4 times activity compared to the 800 K alloy which seemed to be losing activity from the loss of active sites.

The surface alloy made by depositing 0.5 ML Sn on Pt(111) was an attempt to start with less Sn on the surface. Hence, post annealing to the same 1000 K temperature, there would be less Sn on the surface compared to the 1 ML Sn-Pt(111), 1000 K alloy. The reactor studies conducted with this surface produced furfural alcohol at an initial rate of ~2.5 μmol/hr which declined rapidly overtime and dropped to 0.5 μmol/hr at the end of 6 hours corresponding to a conversion of only ~8% (see Figure 3.8). The selectivity to furfural alcohol also started higher at ~70% and dropped to ~30% over the course of 6 hours, all pointing to rapid deactivation of the surface similar to the monometallic Pt(111) surface containing no Sn. This surface demonstrated a higher selectivity to the decarbonylation pathway that produced furan compared to the two other alloys with greater Sn surface coverages. The furan selectivity started off near 18% and dropped off rapidly to

almost zero by the end of 6 hours, again pointing to prompt deactivation. The THF selectivity (~6%) displayed a similar trend to that of furan on this surface as observed in Figure 3.9. In a control experiment, an unannealed surface with 1 ML Sn deposited on Pt(111) displayed no activity whatsoever, indicating that all Pt sites were blocked by the Sn layer which was covering the entire Pt crystal and had no activity for furfural hydrogenation. Figure 3.3-3.9 graphically illustrate the rates of formation and selectivities for furfural alcohol, furan and THF, decomposition on the different surfaces as well as the conversions for the reactor studies.

Selective hydrogenation of crotonaldehyde

Catalytic activity of model Pt-Sn bimetallic alloy were also studied for the selective hydrogenation of crotonaldehyde for the synthesis of the corresponding unsaturated alcohol, crotyl alcohol. Monometallic Pt(111) produced butyraldehyde as the major product, with small amounts of decarbonylation products (propane/propene) detected, while Pt-Sn alloy annealed to 1000 K produced only butyraldehyde. Crotyl alcohol was not detected on either surface. These observations are also consistent with that seen in the literature.[5] Pt-Sn surface alloy annealed to 1000 K was used as the chosen alloy for the rudimentary crotonaldehyde reaction due to its preferable properties displayed in the furfural hydrogenation reaction, giving rise to maximum activity and catalyst stability with good selectivity. Although both the monometallic as well as the bimetallic surface produced butyraldehyde as the major product and had similar conversions, there was a significant difference as seen in Figure 3.10-3.11. The Pt(111) surface produced butyraldehyde at an initial rate of 6 μmol/hr and dropped off rapidly to finally settle near 1 μmol/hr between 4-6 hours, while the Pt-Sn bimetallic surface alloy produced

butyraldehyde at a constant rate of ~2.5 µmol/hr throughout the 6hr experiment with no indication of surface deactivation during this time. Crotonaldehyde selective hydrogenation was also conducted with the 1 ML Sn-Pt(111) 1000 K alloy, using a lower feed concentration of 0.125% crotonaldehyde in balance H_2 at a total flow of 55 sccm, maintaining the rest of the reaction conditions the same, to investigate the effects of the change in the reactant concentration to the selectivity to crotyl alcohol formation. However, butyraldehyde was again the major product, with no crotyl alcohol detected, confirming that neither the Pt(111) surface nor the bimetallic Pt-Sn alloy annealed to 1000 K were able to selectively hydrogenate the C=O bond in crotonaldehyde.

Catalyst characterization

The model catalysts were characterized using XPS, STM, LEED and LEIS techniques. Regardless of the surface Sn coverage on the different alloys, the Pt(4f) and Sn(3d) XPS regions of all the bimetallic surfaces displayed similar trends for both furfural and crotonaldehyde hydrogenation reactions. XPS binding energies for the Pt(4f) and Sn(3d) regions being 71.03 eV and 484.90 eV respectively, verified that both metals were in the metallic, zero oxidation state[55–57] in the as synthesized surface. Depositing Sn on Pt(111) was observed to shift the Pt(4f) signal by 0.1 eV to lower binding energies due to the surface core level shift[58,59] that causes lower coordinated Pt surface sites to have lower binding energy than bulk Pt as observed in Figure 3.12. The Pt(4f) peak intensity returned to almost the clean Pt(4f) signal intensity upon annealing the Sn overlayer, indicating that Sn was driven subsurface as the alloy formed. As observed in Figures 3.12-3.13, no shift in the Pt(4f) or Sn(3d) XPS regions were observed from regular angle XPS spectrum reported here which is dominated by bulk properties due to its reduced surface sensitivity.

Post reaction, the Sn(3d) region displays a 0.2-0.4 eV shift to higher binding energy which is consistent with the presence of oxygen on the surface, evident by comparing the pre and post reaction O(1s) regions. Overall, the O(1s) regions for Pt-Sn bimetallic surfaces had more oxygen post reaction compared to the monometallic Pt(111) surfaces, which was true for both aldehyde hydrogenations as seen in Figure 3.14. The C(1s) regions for all the surfaces analyzed showed similar amounts of carbon deposited on the surfaces post reaction as observed in Figure 3.15. A similar C(1s) signal has been observed upon treatment of the surfaces in pure He at 160 °C. Hence, it can be concluded that the carbon signal observed was due to the overriding effect by the carbon desorbing from the reactor walls condensing on the surfaces upon cooling down to room temperature in inert gas, post reaction. Using dilute feed mixtures with high H_2: aldehyde ratios also further prevents high carbon buildup. The survey region showed the presence of a minor sulfur contamination in the post reaction XPS data indicating that the layer of H_2S used to passivate the reactor walls to kill its activity was desorbing small amounts of H_2S on to the surface. However, the high activity and selectivity of the 1 ML Sn-Pt(111), 1000 K alloy model catalyst with far fewer active sites being comparable with what is reported in the literature for high surface area powder catalysts[51,58,59] stipulated minimal effects from sulfur.

STM studies conducted with 1 ML Sn deposited on Pt(111) at room temperature show nano scale, three dimensional islands of Sn covering the entire surface (Figure 3.16a). Upon annealing the surface to 800 K and 1000 K the islands disappear (Figure 3.16b and 3.16c) indicating that Sn goes subsurface as confirmed with XPS analysis as well. The

fingerprint like patterns observed on the terraces of the alloy surface are evidence for such alloy formation.[60,61]

LEED studies conducted on 1 ML Sn on Pt(111) annealed to 800 K and 1000 K show different ordered crystal structures of PtSn alloys formed on the surface. Upon annealing this surface to 800 K for 1 minute, the $\sqrt{3}x\sqrt{3}$ R30º surface structure was obtained (Figure 3.17), while annealing to 1000 K for 1 minute gave a co-existing mixture of p(2x2) and $\sqrt{3}x\sqrt{3}$ R30º ordered structures[62] as observed in Figure 3.18. In accordance with the LEIS results, the 800 K and 1000 K alloys had Sn surface coverages of 0.43 ML and 0.34 ML respectively, which illustrated that both Pt and Sn were on the top monolayer. This verifies the formation of PtSn ordered surface alloys when subject to annealing treatments. See Table 3.1 for summarized results.

DFT studies were carried out in order to gain insights into the selectivity trends with the monometallic and bimetallic surfaces by investigating the binding of furfural and crotonaldehyde on model monometallic Pt(111) and three ordered, bimetallic, surface alloys, namely, Pt_3Sn (25% Sn , p(2x2) structure) and Pt_2Sn (33% Sn, $\sqrt{3}x\sqrt{3}$ R30º) and PtSn (50% Sn, 110 phase). Calculated binding energies for flat and upright binding configurations of furfural showed that flat binding with lower energy was favored over upright/head on binding for the monometallic Pt(111) slab. As the Sn composition was increased to 25% with the Pt_3Sn surface alloy, the furfural molecule still preferred to lay parallel over the surface while there was no bond formation detected between the Pt_3Sn surface and the furfural molecule as shown in Figure 3.19. As the surface Sn content was increased further to 33% by employing a Pt_2Sn surface, the head on as well as flat binding configurations converged to one. Here, furfural was bound to the surface via the C=O end,

forming an η^1-(O) intermediate that displayed no bonding with the furan ring, which lay almost parallel to the surface. Further increasing the Sn concentration to 50% employing a PtSn surface structure still predicted the formation of a stable η^1-(O) intermediate on the surface. Hence, the most favorable binding configurations for furfural was observed to be flat on Pt(111) while Pt-Sn alloys preferred head on binding in agreement with what is reported in the literature.[51,63]

As shown in Figure 3.20, crotonaldehyde on the other hand preferred flat/linear binding that would activate the C=C bond on most Pt surfaces that were investigated for the DFT studies. According to the DFT calculations, the surface Sn coverage corresponding to the 1 ML Sn on Pt(111), 1000 K alloy (θ_{Sn} = 0.34 ML) forms an η^2-(C,C) intermediate that would explain the experimentally observed favorable hydrogenation of the C=C bond to form butyraldehyde. Further increasing the Sn coverage to 0.5 ML is predicted to energetically favor the formation a flat bound η^2-(C,O) intermediate.

3.4 DISCUSSION

Physical vapor deposition is an ideal method that can be used to deconvolute the effects of Sn-Pt alloy formation from that of Sn oxide induced activity due its capability to be used for metallic Sn deposition. Annealing treatments conducted at 1000 K with a thin overlayer of Sn vapor deposited on Pt(111) are well known to form surface alloys with p(2x2) and $\sqrt{3}$x$\sqrt{3}$ R30º periodicities corresponding to Pt_3Sn(111) face and substitutional Pt_2Sn surface alloy respectively.[42,64,65] Reactor studies combined with LEED analysis showed that the 1 ML Sn on Pt(111) annealed to 800 K and 1000 K containing metallic Pt and Sn had the highest selectivity for furfural alcohol formation with corresponding crystal structures that were pure $\sqrt{3}$x$\sqrt{3}$ R30º and a mixture of p(2x2) + $\sqrt{3}$x$\sqrt{3}$ R30º [62]

respectively. For the 1ML Sn-Pt alloys, the attenuation in the Pt peak observed in LEIS, the recovery of the Pt(4f) peak post annealing in XPS and the Sn island disappearance observed in STM analysis, all confirm that over half a monolayer of Sn deposited is driven subsurface upon being subject to annealing treatments to form Pt-Sn surface alloys. Such ordered Pt-Sn surface alloys are reported to form via annealing due to three major driving forces, the low surface free energy of Sn (0.51 Jm^{-2})[66] compared to that of Pt (2.7 Jm^{-2}),[67] the greater atomic diameter of Sn (3.01 Å) compared to that of Pt (2.77 Å) and the exothermic heat of formation of the alloy.[42] The LEIS Sn coverages determined by the attenuation in the Pt peak were 0.43 ML and 0.34 ML for the 800 K and 1000 K alloy respectively. These results verified that the 800 K annealed surface had more Sn on the surface compared to that of the 1000 K annealed. Additionally, the results further confirm that both catalysts were surface alloys with both metallic Sn and Pt on the topmost monolayer with a 3:4 and 1:2 surface Sn to Pt ratio respectively.

Due to the systematic nature of annealing treatments conducted, the surface Sn coverages of the three ordered alloys should decrease in the following order: 1 ML Sn-Pt(111), 800 K alloy > 1 ML Sn-Pt(111), 1000 K alloy > 0.5 ML Sn-Pt(111), 1000 K alloy. Sn surface coverages obtained for the first two surfaces using LEIS further verify this phenomenon. Furfural alcohol selectivities for these surfaces changing in the same trend as the surface Sn coverage establishes that there is a positive association of the surface Sn coverage with the selectivity to furfural alcohol formation. Furthermore, 1 ML Sn on Pt(111) unannealed surface gave rise to no activity indicating that Sn by itself is not active for the reaction with furfural, thus completely covering the Pt sites with Sn kills the activity completely. In agreement with what was observed for the ordered alloys, supported Pt-Sn

catalysts have also been reported to display monotonically increasing selectivity to C=O bond hydrogenation with increasing surface Sn coverage over a wide surface Sn coverage range with maximum activity detected between 0.4-0.8 Sn:Pt surface ratios; established with XPS analysis.[10,68–70] Simultaneously, DFT calculations demonstrate the increasing preference for head on C=O binding with increasing Sn coverage. Even though all the Sn-Pt alloys were highly selective for furfural alcohol formation at the beginning of the reaction, only one alloy surface composition demonstrated consistent high activity. Hence, Pt-Sn alloy formation is not observed to be the major reason for the consistent high activity for unsaturated alcohol formation which is derived from resistance to surface deactivation.[5,71] The initial selectivity to furfural alcohol formation was however high with all the alloys studied, indicating that alloy formation had a direct positive influence on it.

Rapid increase in the non-selective decomposition percentage as well as decarbonylation pathway to form furan were observed with a simultaneous decrease in the furfural alcohol selectivity for the surfaces with little or no Sn while the 1 ML Sn-Pt(111) alloys annealed to 800 K and 1000 K demonstrated higher, more stable, furfural alcohol selectivity as well as stable decomposition rates. Among the surfaces that rapidly deactivated were the 0.5 ML Sn on Pt(111), 1000 K alloy and the Pt(111) surface (Figure 3.7). The surface Sn: Pt ratio for the 0.5 ML Sn, 1000 K alloy, would be < 1:2 (less than the surface Sn:Pt ratio of 1 ML Sn on Pt(111) 1000 K alloy). The surfaces that deactivated promptly also produced more CO, evident by the higher rates and selectivity to furan formation/decarbonylation pathway. CO poisoning is a commonly known cause for Pt surface deactivation.[72–74] However, XPS results do not indicate the presence of more oxygen on the surfaces with low Sn coverages. In fact, the O(1s) signal was higher for

surfaces containing more Sn. Hence, CO poisoning does not appear to be the main reason for surface deactivation. However, the greater preference to undergo non-selective decomposition observed with surfaces that have low Sn coverages indicate that the loss of active sites from furfural decomposition could be a prime reason for surface deactivation. It was also observed that although the furan formation rate was second highest with the 1 ML Sn-Pt(111), 1000 K alloy; this surface gave rise to stable amounts of furfural alcohol with no sign of deactivation. This indicates that the Sn:Pt ratio for this surface (1:2) is an optimum composition that leads to excellent activity, furfural alcohol selectivity and catalyst stability by possibly suppressing the binding of carbonaceous species that could block the active sites. In agreement with the results from these studies, the Pt to Sn surface ratio is reported to be vital for catalyst stability and longevity.[51]

DFT studies for furfural binding on Pt(111), Pt_3Sn, Pt_2Sn and PtSn revealed that the head-on binding configuration via the C=O bond is preferred, favoring the formation of an η^1-(O) intermediate with increasing Sn concentration. Head on binding of furfural molecules on low activity Cu surfaces have been found to exclusively form an η^1-(O) adsorbed aldehyde intermediate which is the reason for the observed 100% selectivity to furfural alcohol synthesis.[53,79] Electronic effects that are claimed to govern the binding configurations are commonly attributed to be a reason behind the preferred head on C=O binding observed on Pt-Sn catalyst.[32–34] Bimetallic Pd-Cu catalysts that are similar to Pt-Sn catalysts in that they also have an efficient hydrogenation metal (Pd) mixed with a second oxophillic metal (Cu) combination, are claimed to repel the furan ring in furfural from the interactions of metal d electrons with the antibonding orbitals of the furan ring due to electronic effects from alloy formation.[53,79–82] Pt-Sn bimetallic alloys are said to

have similar electronic effects due to their difference in electro negativities (relative electro negativities for Sn and Pt are 1.8 and 2.2 according to the Pauling's scale).[1,3,83] However, regular angle XPS data reveals no evidence for electronic interactions due to the spectrum being dominated by bulk properties and grazing angle XPS will be required to make surface sensitive determinations of Pt-Sn charge transfer interactions. Geometric effects from Pt ensemble dilution is another popular effect ascribed to Pt-Sn alloy formation. [21,27,31] C=C bond hydrogenation as well as C-C bond cleavage (involved in decarbonylation/furan synthesis) are classified as two types of reactions that require contiguous Pt sites.[30,84,85] With the addition of increasing amounts of Sn on the surface, the concurrent dilution of the Pt ensemble is known to suppress said reactions due to the loss of these adjacent Pt sites. [21] The phenomenon of ensemble dilution can be verified by LEED analysis confirming the formation of ordered Sn-Pt surface alloys, while the attenuation in the Pt peak observed in the LEIS analysis upon alloy formation further confirms that the alloy surface had fewer Pt sites compared to Pt(111). Hence, the observed suppression in the selectivity to flat binding could be due to the Pt ensemble dilution by Sn atoms, which is a geometric effect rather than electronic. Furthermore, the furan ring could be pointing away from the surface as the Sn content increases due to steric hindrance from Sn that is known to buckle outwards in these surface alloys.[3,26] The simultaneous increase in head on binding of the C=O oxygen by Sn, which is evident from the XPS O(1s) regions corresponding to the bimetallic alloys being oxygen rich, would cause a combined effect to increase the overall selectivity in favor of furfural alcohol formation.

Crotonaldehyde hydrogenation on the other hand displayed no selectivity to crotyl alcohol formation on monometallic Pt(111) or 1 ML Sn on Pt(111), 1000 K alloy (mixture

of p(2x2) + √3x√3 R30º structures), which demonstrated the highest activity for furfural alcohol formation. Instead, the major product in both cases was butyraldehyde formed from preferably hydrogenating the thermodynamically favored C=C bond. This is observed to correlate well with the η^2-(CC)-intermediate predicted to form over a wide Sn surface coverage (0-0.33 ML) as indicated by the DFT studies performed. The low selectivity to crotyl alcohol formation is also reported elsewhere in the literature with model Pt(111) as well as Pt_3Sn/Pt(111) and Pt_2Sn/Pt(111) ordered alloys.[5] This unfavorable selectivity towards unsaturated alcohol is attributed to crotonaldehyde being a small molecule that does not have steric restrictions from substituted groups near the C=C bond, rendering a greater thermodynamic favorability to C=C bond hydrogenation.[68,86] As with furfural hydrogenation, the monometallic Pt(111) surface that underwent decarbonylation is again the surface that was observed to deactivate promptly. This suggests that the surface selectivity, which is dictated by the Sn:Pt ratio, has an association with the surface deactivation. DFT calculations conducted show that flat binding configuration is preferred by at least -0.5 eV with all the different Pt-Sn compositions starting from monometallic Pt(111) with no Sn. To be more specific, although the flat binding configuration is less favored for the Pt_3Sn, Pt_2Sn and PtSn surfaces compared to that of monometallic Pt(111), in general it was preferred on all tested surfaces compared to head on binding via the C=O bond. Furthermore, High resolution electron energy loss spectroscopy (HREELS) and temperature programmed desorption (TPD) studies combined with DFT calculations have shown that crotonaldehyde can adsorb irreversibly on Pt(111) and Pt_3Sn, Pt_2Sn superstructures formed on Pt(111), giving rise to similar binding configurations and

experimental vibrational fingerprints[1] which could explain the similar trends in selectivities.[4,5,87]

3.5 CONCLUSION

This study investigates the effects of Pt-Sn alloy formation on the selective hydrogenation of two unsaturated aldehydes containing C=C and C=O bonds with different structures using ordered Pt-Sn alloys made on model Pt(111) catalyst to remove structural complexities that derive from support effects. Selective hydrogenation reactions conducted with furfural using low CH:H_2 feed ratios with monometallic Pt(111) and three ordered Pt-Sn alloys demonstrate a direct correlation between the Sn:Pt surface ratio with the selectivity to furfural alcohol formation. Monometallic Pt(111) produced decarbonylation and ring opening products with no selectivity to furfural alcohol formation. Ordered Pt-Sn alloys used as bimetallic catalyst demonstrate an increase in the selectivity to furfural alcohol formation with increasing Sn:Pt surface ratio over the range 0-3:4 with optimum activity and catalyst longevity observed at a 1:2 Sn to Pt ratio. DFT calculations demonstrate the upright binding via the C=O bond to form a η^1-(O) intermediate, which is favored more with the increasing surface Sn coverage. Sn can further increase the preference to bind head on via the C=O bond due to its oxophillic nature, giving rise to the predicted η^1-(O) intermediate, which would explain the furfural alcohol selectivity increase with Sn coverage.

Crotonaldehyde hydrogenation on monometallic Pt(111) and the ordered Pt-Sn alloy preferentially hydrogenated the C=C bond to give rise to the saturated aldehyde, butyraldehyde and did not produce crotyl alcohol. This in agreement with the DFT calculations that demonstrate that the flat binding configuration is preferred on Pt(111) as

well as bimetallic Pt-Sn alloys. This can be explained by the formation of a η^2-(CC)-intermediate over an extended range of Sn surface coverages with crotonaldehyde which is a small molecule that does not give rise to steric hindrance unlike furfural. This is accredited to the linear binding of crotonaldehyde favoring the C=C bond activation. Furthermore, the catalyst also displayed more resistance to deactivation with increasing surface Sn coverage as observed for both unsaturated aldehyde hydrogenations.

The ordered Sn-Pt alloy with a lower Sn coverage undergoing swift surface deactivation as with the monometallic Pt(111) strongly suggests that the Sn: Pt ratio also plays a role in increasing the surface resistance to deactivation. The surface deactivation also has a direct correlation to the selectivity to the decarbonylation pathway as observed for both unsaturated aldehyde hydrogenations. However, CO poisoning which is more likely to occur concurrently with the decarbonylation pathway did not appear to be the reason for the observed surface deactivation. The high initial selectivity observed with all three alloys confirms that alloy formation is a major player in the high selectivity to furfural alcohol formation. However, since not all surface alloys displayed longevity, alloy formation does not appear to be main reason behind resistance to surface deactivation that will ensure consistent activity. Instead, the Sn:Pt ratio that has an optimum value is what seems to be dictating the longevity of the surface. Reduced surface deactivation observed with the Sn-Pt alloy with 1:2 Sn:Pt ratio suggests that the Sn:Pt ratio can be fine-tuned to prevent surface deactivation. The results indicate that the Sn:Pt surface ratio, which governs the adsorption geometry to determine the reaction pathway is the key consideration for designing practical and stable Pt catalysts for this important bio-economy transformation.

Table 3.1: Annealing treatment, crystal structure and LEIS Sn coverages for the 1ML Sn-Pt(111) alloys

Annealing temperature	Annealing time length	Periodicity	LEIS Sn coverage	Sn: Pt ratio
800 K	1 minute	(√3 x √3) R30°	0.43 ML	3:4
1000 K	1 minute	p(2x2) + (√3 x √3) R30° mixture	0.34 ML	1:2

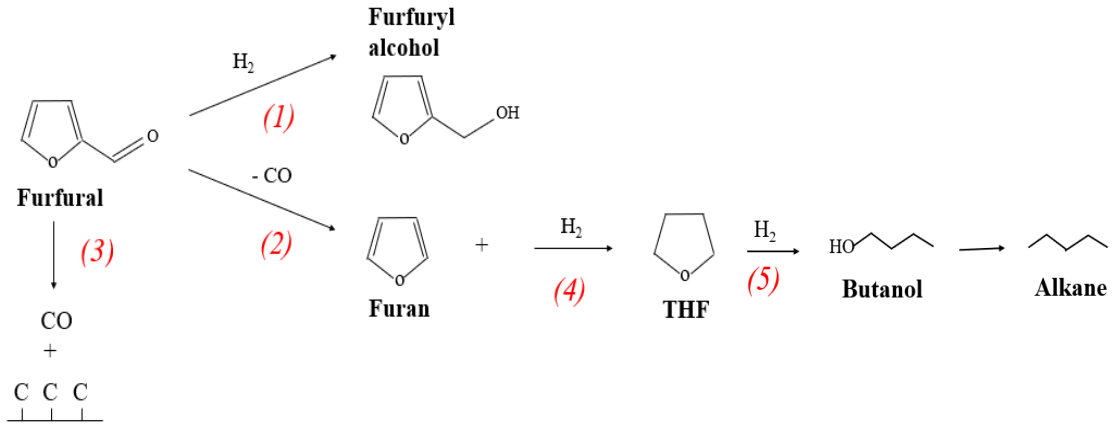

Figure 3.1: Furfural reaction scheme. (1) selective C=O hydrogenation; (2) decarbonylation; (3) nonselective decomposition, (4) ring hydrogenation, (5) ring opening reactions.

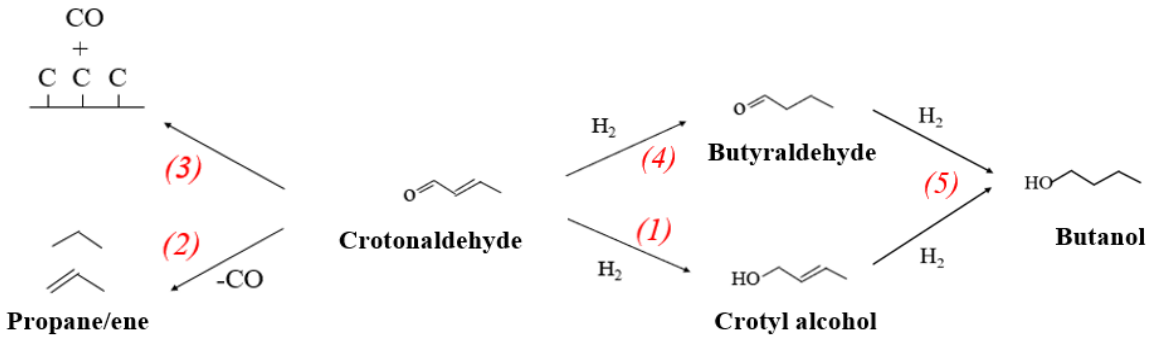

Figure 3.2: Crotonaldehyde reaction scheme. (1) Selective C=O hydrogenation; (2) decarbonylation; (3) nonselective decomposition; (4) olefin bond hydrogenation; (5) secondary hydrogenation.

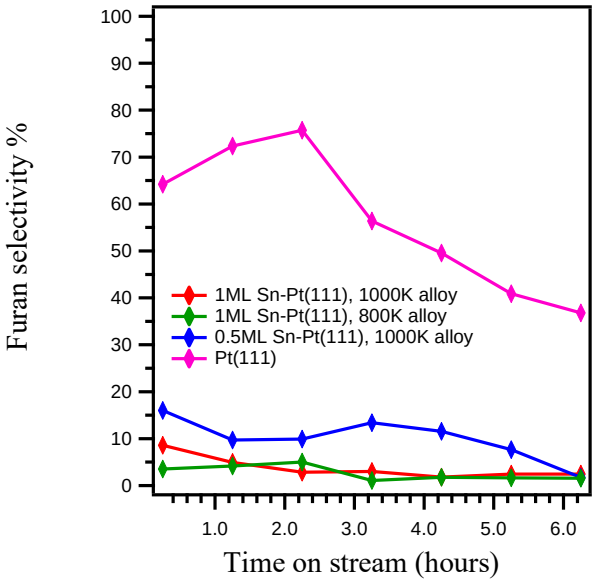

Figure 3.3: Selectivity to furan as a funcntion of time for furfural reaction on different Pt(111) surfaces

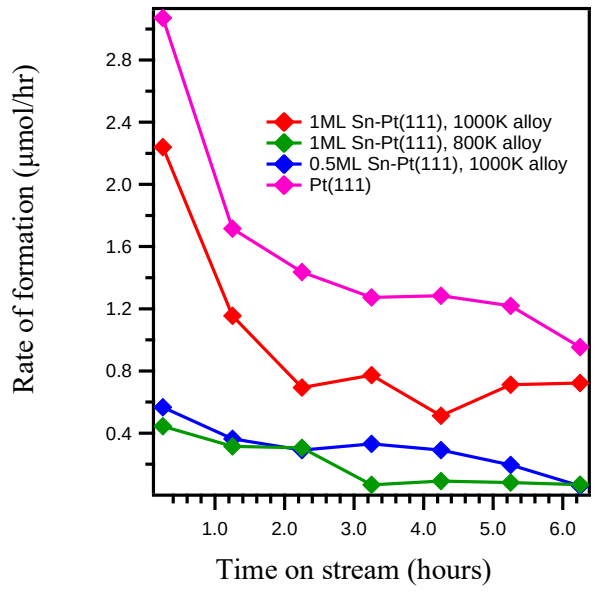

Figure 3.4: Rate of furan formation as a function of time for for furfural reaction on different Pt(111) surface

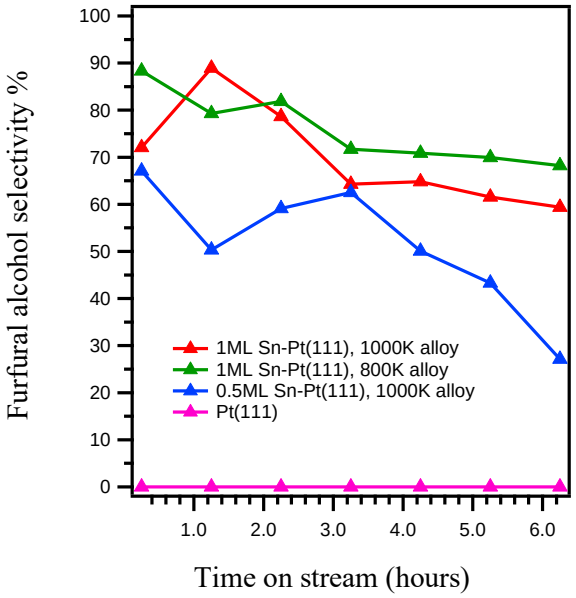

Figure 3.5: Selectivity to furfural alcohol as a function of time for furfural reaction on different Pt(111) surfaces

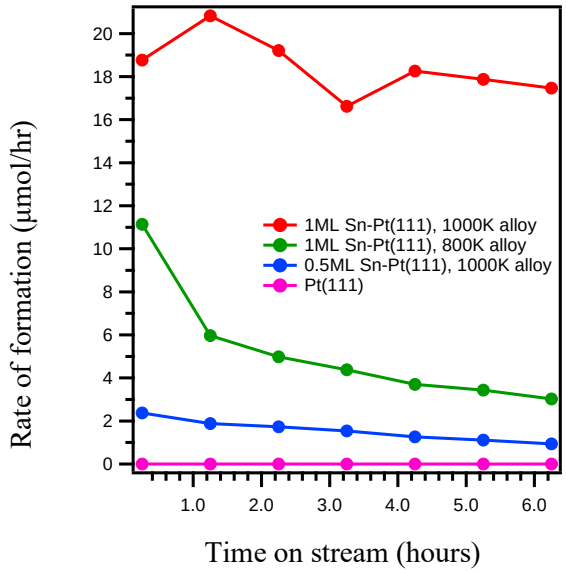

Figure 3.6: Rate of furfural alcohol formation as a function of time for furfural reaction on different Pt(111) surfaces

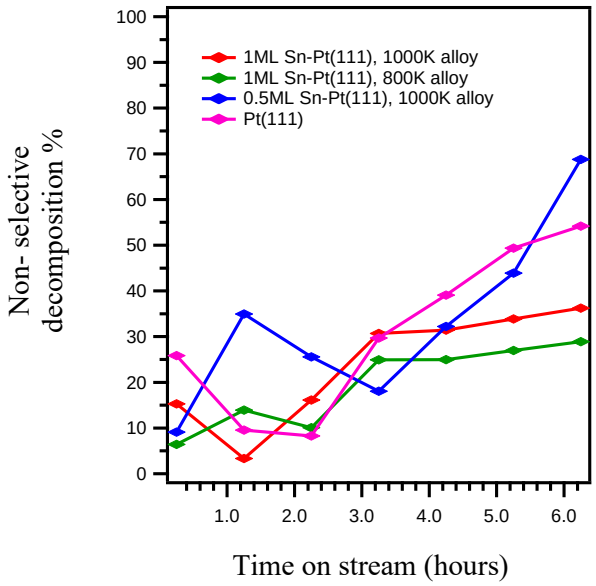

Figure 3.7: Non-selective decomposition as a function of time for furfural reaction on different Pt(111) surfaces

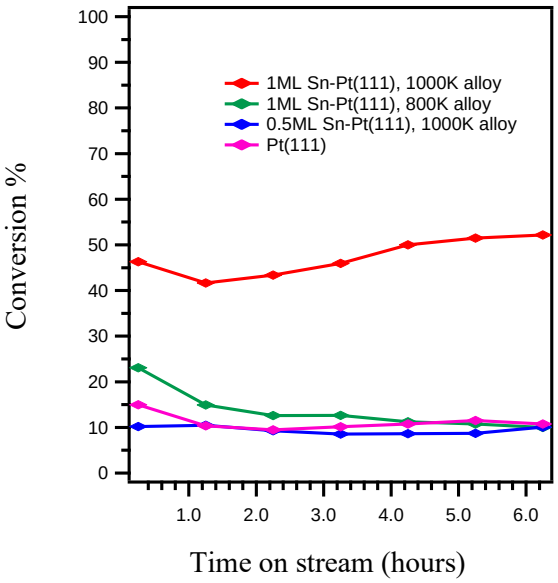

Figure 3.8: Conversion % as a function of time for furfural reaction on different Pt(111) surfaces

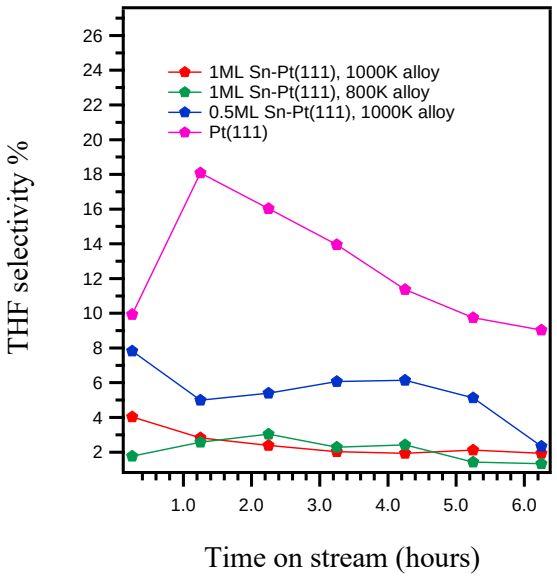

Figure 3.9: THF selectivity % as a function of time for different Pt(111) surfaces

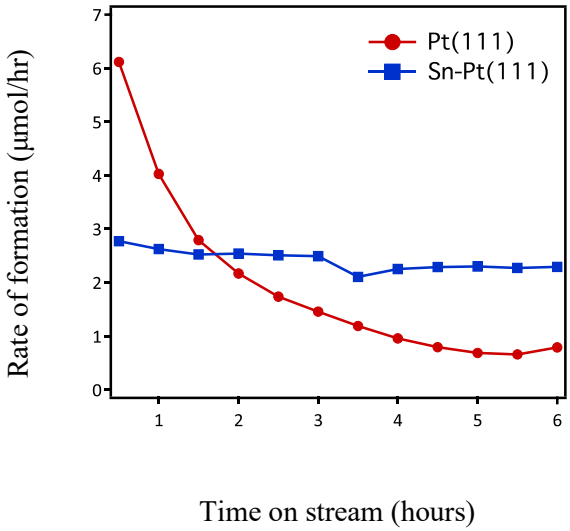

Figure 3.10: Butyraldehyde formation rate as a function of time for crotonaldehyde reaction on different Pt(111) surfaces

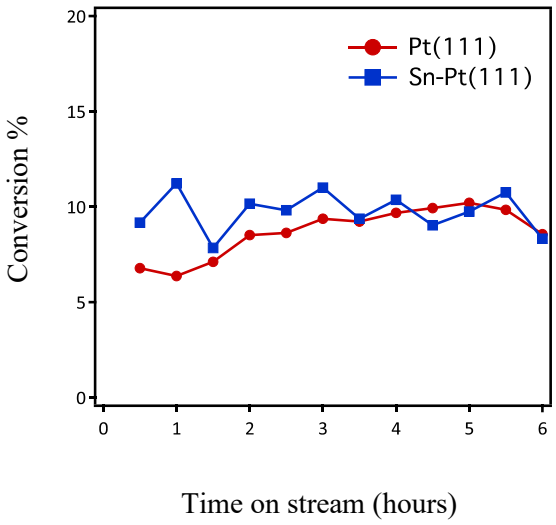

Figure 3.11: Conversion % as a function of time for crotonaldehyde reaction on different Pt(111) surfaces

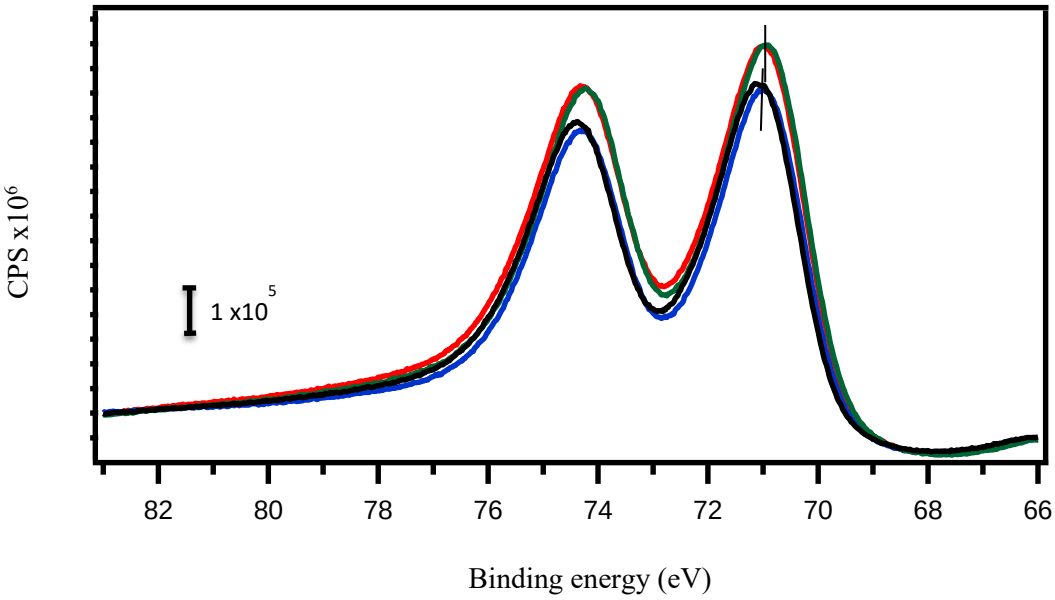

Figure 3.12: Pt(4f) region for clean Pt(111)-red; 1ML Sn-Pt(111)-blue; 1ML Sn-Pt(111) 1000K alloy-green; 1ML Sn-Pt(111) 1000K alloy post reaction-black

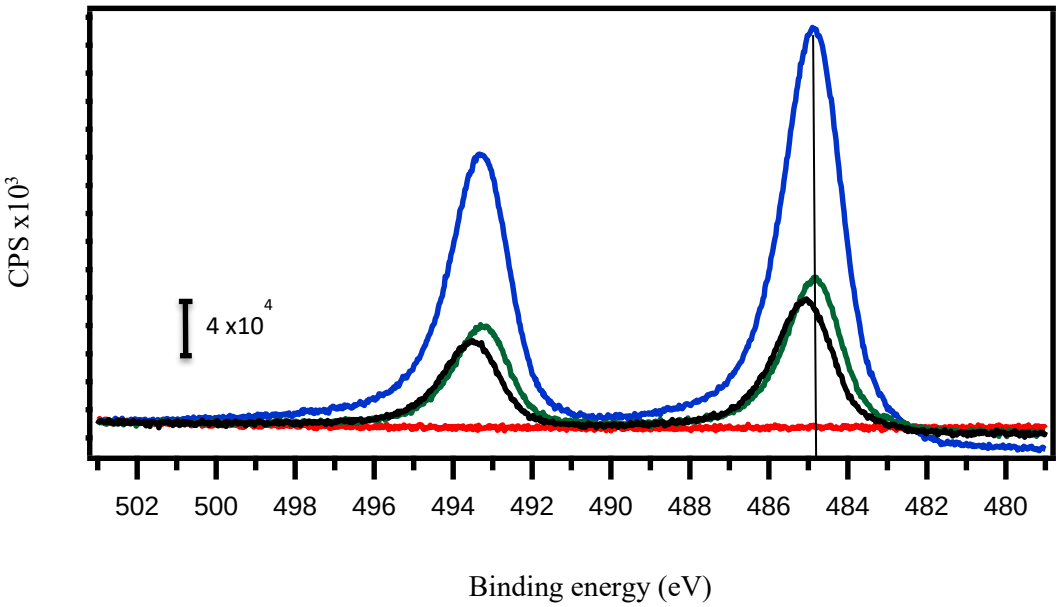

Figure 3.13: Sn(3d) region for clean Pt(111)-red; 1ML Sn-Pt(111)-blue; 1ML Sn-Pt(111) 1000K alloy-green; 1ML Sn-Pt(111), 1000K alloy post reaction-black

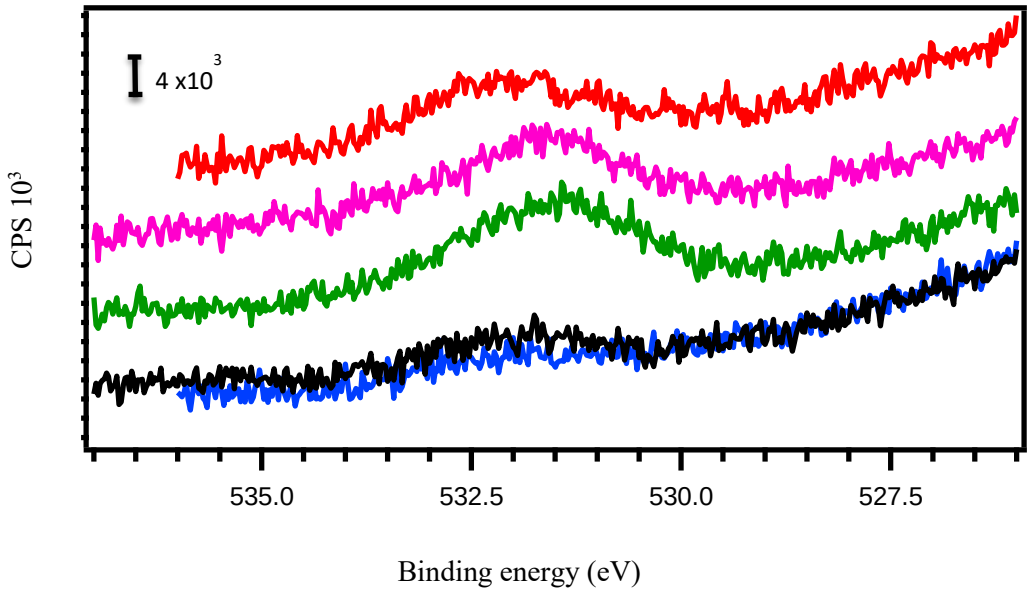

Figure 3.14: post reactions O(1s) region for furfural hydrogenation reactions on 1ML Sn-Pt(111) 1000K alloy-red; 1ML Sn-Pt(111) 800K alloy-pink; Pt(111)-blue; crotonaldehyde hydrogenation reactions on 1ML Sn-Pt(111) 1000K alloy-green and Pt(111)-black

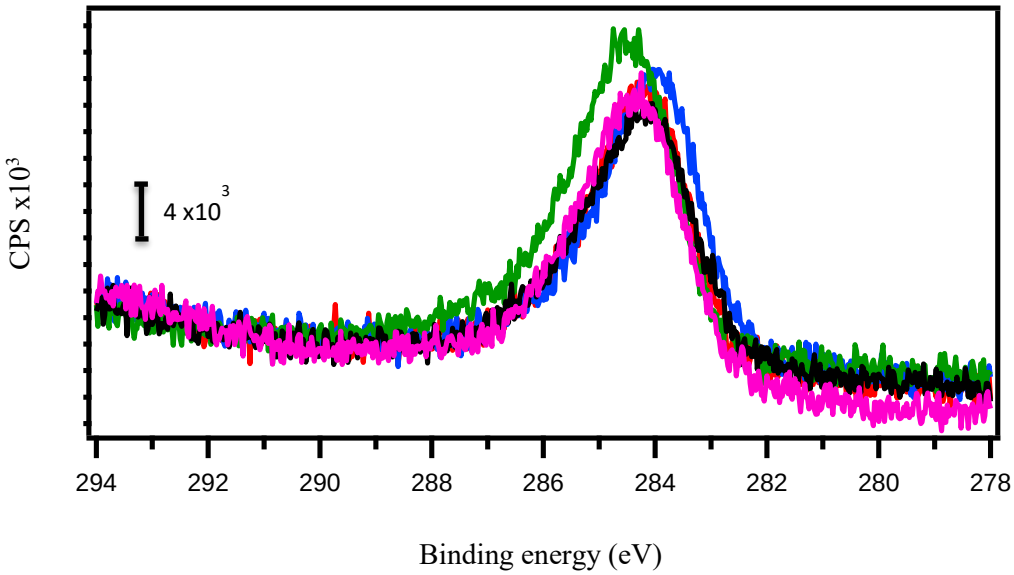

Figure 3.15: post reactions C(1s) region for furfural hydrogenation reactions on 1ML Sn-Pt(111) 1000K alloy-red; 1ML Sn-Pt(111) 800K alloy-pink; Pt(111)-blue; crotonaldehyde hydrogenation reactions on 1ML Sn-Pt(111) 1000K alloy-green and Pt(111)-black

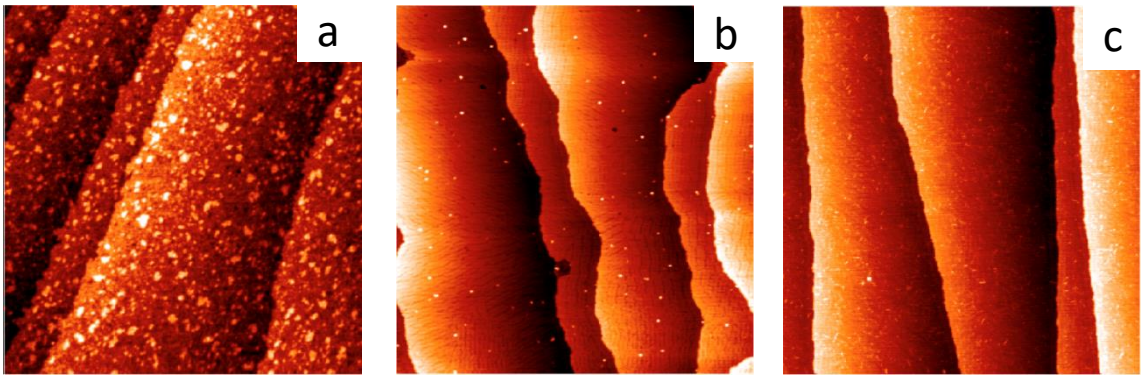

Figure 3.16: STM images of 1ML Sn on Pt(111): a) after room temperature deposition; b) annealed to 800K for 1 minute; c) annealed to 1000K for 1 minute. All images are 110x110 nm.[2]

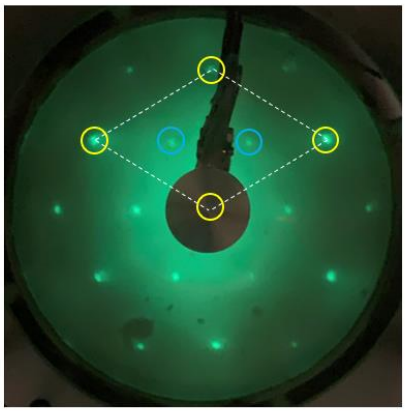

Figure 3.17: 1ML Sn-Pt(111) , 800 K alloy. Blue-(√3 x √3) R30° Sn; Yellow-1x1) Pt.

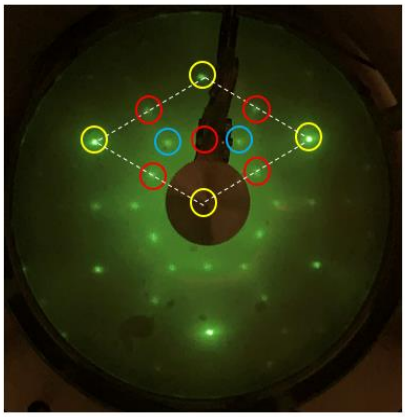

Figure 3.18: 1ML Sn-Pt(111), 1000 K alloy. Blue-(√3 x √3) R30° Sn; Red-p(2x2) Sn; Yellow-(1x1) Pt.

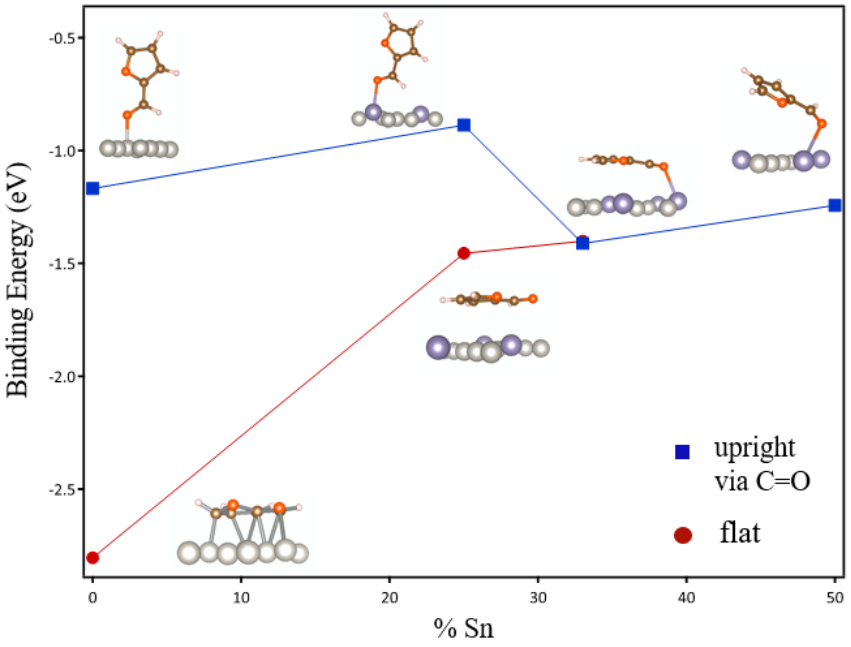

Figure 3.19: Furfural binding configurations on Pt-Sn surfaces as a function of surface Sn coverage.

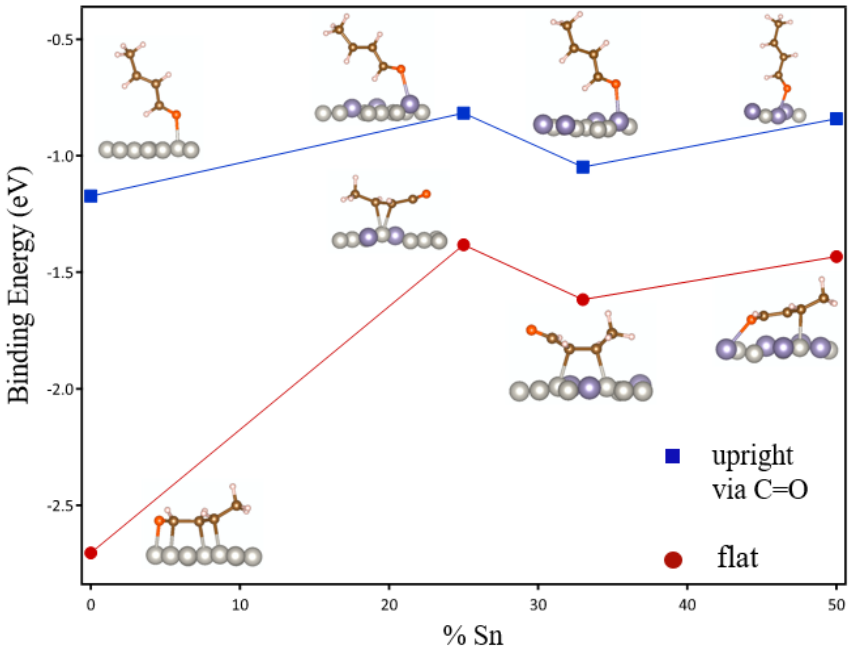

Figure 3.20: Crotonaldehyde binding configurations on Pt-Sn surfaces as a function of surface Sn coverage.

3.6 ACKNOWLEDGEMENTS

I would like to express my sincere gratitude to the national science foundation (NSF) for funding this project, my colleagues at the University of South Carolina, Dr. Sumit Beniwal and Dr. Thathsara Maddumapatabandi for collecting STM, LEED, LEIS data and Dr. Gift Metavarayuth for helping with the reactor and XPS analysis. Additionally, I would like to thank the Henkelman group from U.T. Austin for the theory calculations done for this project.

3.7 REFERENCES

1. Haubrich J, Loffreda D, Delbecq F, et al. Adsorption of α,β-Unsaturated Aldehydes on Pt (111) and Pt - Sn Alloys : II . Crotonaldehyde. *J Phys Chem C*. 2009;(111):13947-13967.
2. Z. Poltarzewski, S. Galvagno, R. Pietropaolo PS. Hydrogenation of α,β-unsaturated aldehydes over Pt-Sn/Nylon. *J Catal*. 1986;102:190.
3. Delbecq F, Sautet P. Influence of Sn additives on the selectivity of hydrogenation of α-β-unsaturated aldehydes with Pt catalysts: A density functional study of molecular adsorption. *J Catal*. 2003;220(1):115-126. doi:10.1016/S0021-9517(03)00249-5
4. Delbecq F, Sautet P. Competitive C=C and C=O Adsorption of α-β unsaturated aldehydes on Pt and Pd surfaces in relation with the selectivity of hydrogenation reactions: A theoretical approach. *J Catal*. 1995;152(2):217-236. doi:10.1006/jcat.1995.1077
5. Jerdev DI, Olivas A, Koel BE. Hydrogenation of crotonaldehyde over Sn/Pt(111) alloy model catalysts. *J Catal*. 2002;205(2):278-288. doi:10.1006/jcat.2001.3452
6. Nagaraja BM, Padmasri AH, David Raju B, Rama Rao KS. Vapor phase selective hydrogenation of furfural to furfuryl alcohol over Cu-MgO coprecipitated catalysts. *J Mol Catal A Chem*. 2007;265(1-2):90-97. doi:10.1016/j.molcata.2006.09.037
7. Kijeński J, Winiarek P, Paryjczak T, Lewicki A, Mikolajska A. Platinum deposited on monolayer supports in selective hydrogenation of furfural to furfuryl alcohol. *Appl Catal A Gen*. 2002;233(1-2):171-182. doi:10.1016/S0926-860X(02)00140-0
8. Nagaraja BM, Siva Kumar V, Shasikala V, et al. A highly efficient Cu/MgO catalyst for vapour phase hydrogenation of furfural to furfuryl alcohol. *Catal Commun*. 2003;4(6):287-293. doi:10.1016/S1566-7367(03)00060-8
9. Mariscal R, Maireles-Torres P, Ojeda M, Sádaba I, López Granados M. Furfural: A renewable and versatile platform molecule for the synthesis of chemicals and fuels. *Energy Environ Sci*. 2016;9(4):1144-1189. doi:10.1039/c5ee02666k

10. Coloma F, Llorca J, Homs N, Ramírez de la Piscina P, Rodríguez-Reinoso F, Sepúlveda-Escribano A. Crotonaldehyde hydrogenation over alumina- and silica-supported Pt-Sn catalysts of different composition. In situ DRIFT study. *Phys Chem Chem Phys*. 2000;2(13):3063-3069. doi:10.1039/b002005m
11. Tamura M, Tokonami K, Nakagawa Y, Tomishige K. Effective NbOx-Modified Ir/SiO2 Catalyst for Selective Gas-Phase Hydrogenation of Crotonaldehyde to Crotyl Alcohol. *ACS Sustain Chem Eng*. 2017;5(5):3685-3697. doi:10.1021/acssuschemeng.6b03060
12. Tamura M, Tokonami K, Nakagawa Y, Tomishige K. Selective Hydrogenation of Crotonaldehyde to Crotyl Alcohol over Metal Oxide Modified Ir Catalysts and Mechanistic Insight. *ACS Catal*. 2016;6(6):3600-3609. doi:10.1021/acscatal.6b00400
13. Lou Y, Zheng Y, Li X, et al. Pocketlike Active Site of Rh 1 / MoS 2 Single-Atom Catalyst for Selective Crotonaldehyde Hydrogenation. *JACS*. 2019. doi:10.1021/jacs.9b06628
14. Taylor MJ, Jiang L, Reichert J, et al. Catalytic Hydrogenation and Hydrodeoxygenation of Furfural over Pt (111); a Model System for the Rational Design and Operation of Practical Biomass Conversion Catalysts. *J. Phys. Chem. C* 2017;(111). doi:10.1021/acs.jpcc.7b01744
15. Pino N, López D, Espinal JF. Thermochemistry and kinetic analysis for the conversion of furfural to valuable added products. *J Mol Model*. 2019;25(1):1-10. doi:10.1007/s00894-018-3908-0
16. Mariscal R, Ojeda M. Furfural: a renewable and versatile platform molecule for the synthesis of chemicals and fuels. *Energy Environ Sci*. 2016;9:1144-1189. doi:10.1039/c5ee02666k
17. Guo P, Liao S, Tong X. Heterogeneous Nickel Catalysts Derived from 2D Metal-Organic Frameworks for Regulating the Selectivity of Furfural Hydrogenation. *ACS Omega*. 2019. doi:10.1021/acsomega.9b02443
18. Jiang Z, Wan W, Lin Z, Xie J, Chen JG. Understanding the Role of M/Pt(111) (M = Fe, Co, Ni, Cu) Bimetallic Surfaces for Selective Hydrodeoxygenation of Furfural. *ACS Catal*. 2017;7(9):5758-5765. doi:10.1021/acscatal.7b01682
19. Concepción P, Pérez Y, Hernández-Garrido JC, Fajardo M, Calvino JJ, Corma A. The promotional effect of Sn-beta zeolites on platinum for the selective hydrogenation of α,β-unsaturated aldehydes. *Phys Chem Chem Phys*. 2013;15(29):12048-12055. doi:10.1039/c3cp50519g
20. Alexeev OS, Gates BC. Supported Bimetallic Cluster Catalysts. *Ind Eng Chem Res*. 2003;42(8):1571-1587. doi:10.1021/ie020351h
21. Coloma F, Sepúlveda-Escribano A, Fierro JLG, Rodríguez-Reinoso F. Crotonaldehyde hydrogenation over bimetallic Pt - Sn catalysts supported on pregraphitized carbon black. Effect of the Sn/Pt atomic ratio. *Appl Catal A Gen*. 1996;136(2):231-248. doi:10.1016/0926-860X(95)00259-6
22. Bodke AS, Olschki DA, Schmidt LD, Ranzi E. High selectivities to ethylene by partial oxidation of ethane. *Science (80-)*. 1999;285(5428):712-715. doi:10.1126/science.285.5428.712
23. Szanyi, J. (1994). n-Butane Hydrogenolysis at Sn/Pt(111) Surface Alloys. *J Catal*, 149(2), 438–448. doi:10.1006/jcat.1994.1310

24. Pham HN, Sattler JJHB, Weckhuysen BM, Datye AK. Role of Sn in the Regeneration of Pt/γ-Al2O3Light Alkane Dehydrogenation Catalysts. *ACS Catal*. 2016;6(4):2257-2264. doi:10.1021/acscatal.5b02917
25. Cortright, R. D., & Dumesic, J. A. Microcalorimetric, Spectroscopic, and Kinetic Studies of Silica Supported Pt and Pt/Sn Catalysts for Isobutane Dehydrogenation. *J Catal. 1994*, 148(2), 771–778. doi:10.1006/jcat.1994.1263
26. Panja C, Saliba NA, Koel BE. Coking resistance of Pt – Sn alloys probed by acetylene chemisorption. *Catal Lett*. 2000;68:175-180.
27. Altmann L, Wang X, et al. Influence of Sn content on the hydrogenation of crotonaldehyde catalysed by colloidally prepared. *Phys Chem Chem Phys*. 2015. doi:10.1039/C5CP00280J
28. Rong H, Niu Z, Zhao Y, et al. Structure Evolution and Associated Catalytic Properties of Pt À Sn Bimetallic Nanoparticles. *Chem Eur J*. 2015:12034-12041. doi:10.1002/chem.201501442
29. Suzuki H, Takaya Y, Takemori T, Tanaka M. Selective Carbon-Carbon Bond Cleavage of Cyclopentadiene on a Trinuclear Ruthenium Pentahydride Complex. *J Am Chem Soc*. 1994;116(23):10779-10780. doi:10.1021/ja00102a051
30. Santen RA, Leeuwen PWNM et al. Catalysis: An Integrated Approach. Volume 123. Edition 2. New york: *Elsevier Science; 1999.* https://books.google.com/books?id=g1A-mi726QwC&printsec=frontcover&source=gbs_ge_summary_r&cad=0#v=onepage&q&f=false Accessed January 29, 2020.
31. Merlo AB, Santori GF, Sambeth J, Siri GJ, Casella ML, Ferretti OA. Hydrogenation of crotonaldehyde and butyraldehyde on silica supported Pt and PtSn catalysts: A drifts study. *Catal Commun*. 2006;7(4):204-208. doi:10.1016/j.catcom.2005.11.002
32. Nakagawa Y, Tamura M, Tomishige K. Catalytic reduction of biomass-derived furanic compounds with hydrogen. *ACS Catal*. 2013;3(12):2655-2668. doi:10.1021/cs400616p
33. Sankar M, Dimitratos N, Miedziak PJ, Wells PP, Kiely CJ, Hutchings GJ. Designing bimetallic catalysts for a green and sustainable future. *Chem Soc Rev*. 2012;41(24):8099-8139. doi:10.1039/c2cs35296f
34. Chen YZ, Wei SW, Wu KJ. Effect of promoter on selective hydrogenation of α,β-unsaturated aldehydes over cobalt borides. *Appl Catal A, Gen*. 1993;99(2):85-96. doi:10.1016/0926-860X(93)80092-5
35. Merlen E, Beccat P, Bertolini JC, Delichère P, Zanier N, Didillon B. Characterization of bimetallic Pt-Sn/Al2O3catalysts: Relationship between particle size and structure. *J Catal*. 1996;159(1):178-188. doi:10.1006/jcat.1996.0077
36. Völter J, Lietz G, Uhlemann M, Hermann M. Conversion of cyclohexane and n-heptane on PtPb Al2O3 and PtSn Al2O3 bimetallic catalysts. *J Catal*. 1981;68(1):42-50. doi:10.1016/0021-9517(81)90038-5
37. Duke AS, Xie K, Monnier JR, Chen DA. Superior long-term activity for a Pt-Re alloy compared to Pt in methanol oxidation reactions. *Surf Sci*. 2017;657:35-43. doi:10.1016/j.susc.2016.11.007

38. Duke AS, Xie K, Brandt AJ, et al. Understanding Active Sites in the Water-Gas Shift Reaction for Pt-Re Catalysts on Titania. ACS Catal. 2017, 7(4), 2597–2606. doi:10.1021/acscatal.7b00086
39. Tenney SA, Xie K, Monnier JR, et al. Novel recirculating loop reactor for studies on model catalysts: CO oxidation on Pt/TiO2(110). *Rev Sci Instrum*. 2013;84(10). doi:10.1063/1.4824142
40. Tenney SA, He W, Roberts CC, et al. CO-Induced diffusion of Ni atoms to the surface of Ni-Au clusters on TiO2(110). *J Phys Chem C*. 2011;115(22):11112-11123. doi:10.1021/jp2014258
41. Tenney SA, Ratliff JS, Roberts CC, et al. Adsorbate-induced changes in the surface composition of bimetallic clusters: Pt-Au on TiO2(110). *J Phys Chem C*. 2010;114(49):21652-21663. doi:10.1021/jp108939h
42. Paffett MT, Windham RG. Surface modification of Pt(111) by Sn adatoms: Evidence for the formation of ordered overlayers and surface alloys. *Surf Sci*. 1989;208(1-2):34-54. doi:10.1016/0039-6028(89)90035-6
43. Xiong K, Wan W, Chen JG. Reaction pathways of furfural, furfuryl alcohol and 2-methylfuran on Cu(111) and NiCu bimetallic surfaces. *Surf Sci*. 2016;652(111):91-97. doi:10.1016/j.susc.2016.02.011
44. Abid, M., Ammari, F., Liberkova, K., & Touroude, R. Selective hydrogenation of unsaturated aldehydes into unsaturated alcohols: Role of metal-support interactions in platinum catalysts. *Studies in Surface Science and Catalysis*. 2003; 267–270. doi:10.1016/s0167-2991(03)80211-2
45. Selishcheva SA, Smirnov AA, Fedorov A V., et al. Highly active CuFeAl-containing catalysts for selective hydrogenation of furfural to furfuryl alcohol. *Catalysts*. 2019;9(10):1-20. doi:10.3390/catal9100816
46. Park JB, Conner SF, Chen DA. Bimetallic Pt - Au Clusters on TiO_2 (110): Growth , Surface Composition , and Metal - Support Interactions. J Phy Chem, 2008;2(110):5490-5500.
47. Kresse G, Furthmüller J. Efficiency of ab-initio total energy calculations for metals and semiconductors using a plane-wave basis set. *Comput Mater Sci*. 1996;6(1):15-50. doi:10.1016/0927-0256(96)00008-0
48. Kresse G, Furthmüller J. Efficient iterative schemes for ab initio total-energy calculations using a plane-wave basis set. *Phys Rev B - Condens Matter Mater Phys*. 1996;54(16):11169-11186. doi:10.1103/PhysRevB.54.11169
49. Blöchl PE. Projector augmented-wave method. *Phys Rev B*. 1994;50(24):17953-17979. doi:10.1103/PhysRevB.50.17953
50. Perdew JP, Burke K, Ernzerhof M. Generalized gradient approximation made simple. *Phys Rev Lett*. 1996;77(18):3865-3868. doi:10.1103/PhysRevLett.77.3865
51. Maligal-Ganesh R V., Xiao C, Goh TW, et al. A Ship-in-a-Bottle Strategy to Synthesize Encapsulated Intermetallic Nanoparticle Catalysts: Exemplified for Furfural Hydrogenation. *ACS Catal*. 2016;6(3):1754-1763. doi:10.1021/acscatal.5b02281
52. Chen YZ, Wei SW, Wu KJ. Effect of promoter on selective hydrogenation of α,β-unsaturated aldehydes over cobalt borides. *Appl Catal A, Gen*. 1993;99(2):85-96. doi:10.1016/0926-860X(93)80092-5

53. Sitthisa S, Resasco DE. Hydrodeoxygenation of furfural over supported metal catalysts: A comparative study of Cu, Pd and Ni. *Catal Letters*. 2011;141(6):784-791. doi:10.1007/s10562-011-0581-7
54. Dong H, Zheng Y, Hu P. DFT study of furfural conversion on a Re/Pt bimetallic surface: Synergetic effect on the promotion of hydrodeoxygenation. *Phys Chem Chem Phys*. 2019;21(16):8384-8393. doi:10.1039/c8cp07806h
55. Jerdev DI, Koel BE. Oxidation of ordered Pt-Sn surface alloys by O2. *Surf Sci*. 2001;492(1-2):106-114. doi:10.1016/S0039-6028(01)01407-8
56. Nyholm R, Berndtsson A, Martensson N. Core level binding energies for the elements Hf to Bi (Z=72-83). *J Phys C Solid State Phys*. 1980;13(36). doi:10.1088/0022-3719/13/36/009
57. Virnovskaia A, Jørgensen S, Hafizovic J, et al. In situ XPS investigation of Pt(Sn)/Mg(Al)O catalysts during ethane dehydrogenation experiments. *Surf Sci*. 2007;601(1):30-43. doi:10.1016/j.susc.2006.09.002
58. Walter AL, Schiller F, Corso M, et al. X-ray photoemission analysis of clean and carbon monoxide-chemisorbed platinum(111) stepped surfaces using a curved crystal. *Nat Commun*. 2015;6. doi:10.1038/ncomms9903
59. Baetzold RC, Apai G, Shustorovich E, Jaeger R. Surface core-level shifts for Pt single-crystal surfaces. *Phys Rev B*. 1982;26(8):4022-4027. doi:10.1103/PhysRevB.26.4022
60. Merlo AB, Vetere V, Ruggera JF, Casella ML. Bimetallic PtSn catalyst for the selective hydrogenation of furfural to furfuryl alcohol in liquid-phase. *Catal Commun*. 2009;10(13):1665-1669. doi:10.1016/j.catcom.2009.05.005
61. O'Driscoll Á, Curtin T, Hernández WY, Van Der Voort P, Leahy JJ. Hydrogenation of Furfural with a Pt–Sn Catalyst: The Suitability to Sustainable Industrial Application. *Org Process Res Dev*. 2016;20(11):1917-1929. doi:10.1021/acs.oprd.6b00228
62. Wang ZT, Darby MT, Therrien AJ, et al. Preparation, Structure, and Surface Chemistry of Ni-Au Single Atom Alloys. *J Phys Chem C*. 2016;120(25):13574-13580. doi:10.1021/acs.jpcc.6b03473
63. Hoster HE, Bergbreiter A, Erne PM, Hager T, Rauscher H, Behm RJ. PtxRu1-x/Ru(0001) surface alloys - Formation and atom distribution. *Phys Chem Chem Phys*. 2008;10(25):3812-3823. doi:10.1039/b802169d
64. Batzill M, Beck DE, Koel BE. Electronic contrast in scanning tunneling microscopy of Sn-Pt(111) surface alloys. *Surf Sci*. 2000;466(1-3). doi:10.1016/S0039-6028(00)00803-7
65. Liu B, Cheng L, Curtiss L, Greeley J. Effects of van der Waals density functional corrections on trends in furfural adsorption and hydrogenation on close-packed transition metal surfaces. *Surf Sci*. 2014;622:51-59. doi:10.1016/j.susc.2013.12.001
66. Paffett MT, Gebhard SC, Windham RG, Koel BE. Chemisorption of ethylene on ordered Sn/Pt(111) surface alloys. *Surf Sci*. 1989;223(3):449-464. doi:10.1016/0039-6028(89)90673-0
67. Galeotti M, Atrei A, Bardi U, Rovida G, Torrini M. Surface alloying at the SnPt(111) interface: a study by x-ray photoelectron diffraction. *Surf Sci*. 1994;313(3):349-354. doi:10.1016/0039-6028(94)90055-8

68. Rice CM, Eppelsheimer DS, McNeil MB. Surface tension of solid tin. *J Appl Phys*. 1966;37(13):4766-4768. doi:10.1063/1.1708134
69. Krishnan KM. Fundamentals and Applications of Magnetic. New york: OXFORD; 2016. https://www.google.com/books/edition/Fundamentals_and_Applications_of_Magneti/QBo1DQAAQBAJ?hl=en&gbpv=1&printsec=frontcover Accessed February 2, 2020.
70. Santori GF, Casella ML, Siri GJ, Ferretti OA, Moglioni A, Iglesias GM. Hydrogenation of carbonylic compounds on Pt/SiO2 catalysts modified with SnBu4. *Stud Surf Sci Catal*. 2000;130 C:2063-2068. doi:10.1016/s0167-2991(00)80772-7
71. Galvagno S, Milone C, Donato A, Neri G, Pietropaolo R. Hydrogenation of citral over Ru-Sn/C. *Catal Letters*. 1993;17(1-2):55-61. doi:10.1007/BF00763927
72. Hou F, Zhao H, Song H, et al. Insight into the structure evolution and the associated catalytic behavior of highly dispersed Pt and PtSn catalysts supported on La 2 O 2 CO 3 nanorods. *RSC Adv*. 2017;7(77):48649-48661. doi:10.1039/c7ra10084a
73. Haubrich J, Loffreda D, Delbecq F, et al. Adsorption of r , -Unsaturated Aldehydes on Pt (111) and Pt - Sn Alloys : II . Crotonaldehyde. 2009;(111):13947-13967.
74. Trens P, Durand R, Coq B, Coutanceau C, Rousseau S, Lamy C. Poisoning of Pt/C catalysts by CO and its consequences over the kinetics of hydrogen chemisorption. *Appl Catal B Environ*. 2009;92(3-4):280-284. doi:10.1016/j.apcatb.2009.08.004
75. Grunes J, Zhu J, Yang M, Somorjai GA. CO poisoning of ethylene hydrogenation over Pt catalysts: A comparison of Pt(111) single crystal and Pt nanoparticle activities. *Catal Letters*. 2003;86(4):157-161. doi:10.1023/A:1022628404888
76. Chung DY, Kim H Il, Chung YH, et al. Inhibition of CO poisoning on Pt catalyst coupled with the reduction of toxic hexavalent chromium in a dual-functional fuel cell. *Sci Rep*. 2014;4. doi:10.1038/srep07450
77. Sitthisa S, Sooknoi T, Ma Y, Balbuena PB, Resasco DE. Kinetics and mechanism of hydrogenation of furfural on Cu/SiO2catalysts. *J Catal*. 2011;277(1):1-13. doi:10.1016/j.jcat.2010.10.005
78. Sitthisa S, Pham T, Prasomsri T, Sooknoi T, Mallinson RG, Resasco DE. Conversion of furfural and 2-methylpentanal on Pd/SiO2and Pd-Cu/SiO2catalysts. *J Catal*. 2011;280(1):17-27. doi:10.1016/j.jcat.2011.02.006
79. Chen S, Wojcieszak R, Dumeignil F, Marceau E, Royer S. How Catalysts and Experimental Conditions Determine the Selective Hydroconversion of Furfural and 5-Hydroxymethylfurfural. *Chem Rev*. 2018;118(22):11023-11117. doi:10.1021/acs.chemrev.8b00134
80. Shi Y, Zhu Y, Yang Y, Li YW, Jiao H. Exploring Furfural Catalytic Conversion on Cu(111) from Computation. *ACS Catal*. 2015;5(7):4020-4032. doi:10.1021/acscatal.5b00303
81. Hammer B, Nørskov JK. Theoretical surface science and catalysis—calculations and concepts. *Adv Catal*. 2000;45(C):71-129. doi:10.1016/S0360-0564(02)45013-4

82. Cerveny L. Catalytic Hydrogenation. Volume 27. Amsterdam: *Elsevier science*-1986. https://books.google.com/books?id=IiZVzDsTDc0C&printsec=frontcover&source=gbs_ge_summary_r&cad=0#v=onepage&q&f=false Accessed January 29, 2020.
83. Sheldon RA. Bekkum H. Fine Chemicals through Heterogeneous Catalysis. New york*: WILEY-VCH*; 2001. https://books.google.com/books?id=RW8griumzqcC&printsec=frontcover&source=gbs_ge_summary_r&cad=0#v=onepage&q&f=false Accessed January 29, 2020.
84. Marinelli TBLW, Nabuurs S, Ponec V. Activity and selectivity in the reactions of substituted α,β-Unsaturated aldehydes. *J Catal*. 1995;151(2):431-438. doi:10.1006/jcat.1995.1045
85. De Jesús JC, Zaera F. Adsorption and thermal chemistry of acrolein and crotonaldehyde on Pt(111) surfaces. *Surf Sci*. 1999;430(1):99-115. doi:10.1016/S0039-6028(99)00406-9

CHAPTER 4

SYNTHESIS OF BIMETALLIC MOF THIN FILMS FOR FUNDAMANTAL STUDIES

4.1 INTRODUCTION

Metal organic frameworks (MOFs) are an emerging class of crystalline, high surface area, porous material which consist of metal centers with organic linkers bound to it.[1–4] The metal centers acts as joints while the organic linkers play the role of struts forming the framework.[5] These materials have potential applications in the areas of gas storage[5,6], gas adsorption/separation[7–10], air purification[5,11], chemical sensing[5,12], optical devices[5,13,14], energy conversion/storage[15,16] and heterogeneous catalysis.[8,17–20] The chemical versatility that enables various applications are a consequence of the tunable properties of MOFs that arise from the ability to use a wide range of metal-ligand combinations to control the structure, geometry and distribution.[6,14] Second metal incorporation is one such method by which the properties of MOFs can be tuned. Node metal replacement, metal node extension and metal coordination to the linker are three common pathways by which a second metal can be integrated in to an existing framework.[3,21–23] Out of these methods, node metal replacement using solvothermal techniques is one of the least complicated options where the second metal will replace the existing metal in the same coordination environment.[3,22] Previous studies conducted by the Chen group in collaboration with the Shustova group investigated the tunable electronic properties and catalytic activity of CuBTC powder MOFs and its bimetallic derivatives synthesized using solvothermal reactions.[19,24] HKUST-1 MOFs that will be identified as CuBTC in this work has a unit cell formula

$Cu_3(BTC)_2$ and forms a paddle wheel structure where the two Cu(II) ions in the binuclear nodes are each coordinated to four carboxylic oxygen atoms from four BTC^{3-} ligands that are completely deprotonated, forming dimeric units,[25,26] as depicted in Figure 4.1. Water/solvent molecules can also bind to the metal nodes at the axial unsaturated metal sites along the Cu-Cu vector giving rise to an octahedral geometry.[24,25,27–29]

The incorporation of a second metals such as Rh, Co or Zn via metal node replacement have been studied in the past in order to synthesize bimetallic powder MOFs with an isostructural framework to CuBTC as illustrated in Figure 4.2.[19,24] These MOFs have invaluable applications in heterogeneous catalysis[19] and electronics.[19,24] However, many complications can arise when conducting thorough analysis with high surface area powder MOFs making it difficult to distinguish between the nature of interactions of the inner surfaces of the pores with guest molecules and that of the outer MOF surface. As an example, with complex powders it is difficult to conduct controlled, systematic studies for kinetic insights due to the diffusion of gaseous molecules into pores.[30] Furthermore, the three-dimensional nature of the MOF powders can also hinder use of standard spectroscopic techniques for elaborate characterization. For example, X-ray photoelectron spectroscopy of the powder MOFs is complicated by the insulating nature of the MOFs, which can give rise to severe charging issues and the complex nature of the powder that can give rise to background features.[31] On the other hand, bulk sensitive techniques such as IR spectroscopy makes it impossible to be used to distinguish between surface and pore interactions of guest molecules.[31] In this context, the synthesis of homogenous thin films of MOFs that can be considered as 2D analogues or model systems can unlock the doors to a wide variety of in-depth surface science techniques that are available to meticulously

study and characterize the surface components present in the complex 3D material that have ample applications.[21,22,31] By growing the insulating MOF films on semiconducting substrates such as Si, the charging issues can be reduced, while the growth of few layers of film will eliminate the formation of deeper pores to significantly eliminate interaction of guest molecules with the MOF pores. Furthermore, MOFs are required to be made in the form of thin films to enable their usage for certain applications such as membranes, semiconducting material and photovoltaics.[16,31–33]

In contrast to the established solvothermal synthesis where the primary building blocks are mixed together and left to react under solvothermal conditions, sequential, layer-by-layer techniques are employed to grow thin film analogues of the high surface area powder MOFs. Here, sequential dip coating is performed by periodic immersion of a substrate into separate precursor solutions, one at a time to enable serial growth for bottom up synthesis as illustrated in Figure 4.3.[16,34–36] The substrate is rinsed with solvent in between the precursor dip coating steps to remove excess precursor molecules that did not get incorporated in the structure before putting down the next component.[34,35] Previous studies have demonstrated the successful growth of bimetallic CuCoBTC MOF thin films using a layer-by layer synthesis of CuBTC followed by metal node replacement in $CoCl_2$ solution.[30] The current work demonstrates that a similar growth technique can be used to synthesize thin films of CuRhBTC MOFs that have excellent hydrogenation properties,[19] in order to enable fundamental kinetic investigations with this simplified analogue of the CuRhBTC powder material.

4.2 EXPERIMENTAL

Materials

$Cu(CH_3COO)_2 \cdot H_2O$ (>95%, TCI America), 1,3,5-benzenetricarboxylic acid (98%, Alfa Aesar), $RhCl_3 \cdot H_2O$ (98.98%, Engelhard Chemicals), $Rh_2(CH_3COO)_4$ (99.99%, Sigma-Aldrich), ethanol (200 proof, Decon Laboratories), *N,N′*-dimethylformamide (ACS grade, BDH), tetrachloroethylene (99.9%, BDH), acetone (≥99.5%, Sigma-Aldrich), and methanol (≥99.8%, Sigma-Aldrich), p-type Si(100) substrate (University Wafer).

Monometallic MOF film preparation

Copper acetate and 1,3,5-benzenetricarboxylic acid (H_3BTC) solutions made in 1mM concentrations in ethanol were used as the precursors for Cu and benzynetricarboxylic (BTC) acid ligand respectively for dip coating thin films of binodal CuBTC MOF on Al_2O_3 (2.5 nm layer) sputter deposited Si substrate. Al_2O_3-Si wafers were cut in to roughly 1.0 cm x 1.2 cm rectangles using a diamond scribe and cleaned by sonicating in trichloroethylene, acetone and methanol for 15 min each. Sequential dip coating was performed using a homemade robotic arm that is shown in Figure 4.4, which was used to dip the Al_2O_3-Si wafer in copper acetate and H_3BTC solutions for 1 min each. A rinsing step with ethanol and a drying step with $N_{2(g)}$ were carried out for 15s each, in between the precursor solution dips to remove excess physisorbed film off the Si substrate.

MOF film Transmetallation

In order to prepare bimetallic films containing both Cu and Rh in the binuclear nodes, the premade monometallic, binuclear CuBTC film was submerged in 0.5-1 mL $RhCl_3$/Rh acetate solutions made using ethanol as the solvent. Ethanol was chosen as the exchange solvent because CuRhBTC MOF powders have been successfully synthesized

by the Shustova group using ethanol as a solvent.[19] The amount of Rh exchanged was attempted to control by changing the $RhCl_3$ concentration (0.001 M-0.03M), the exchange temperature (25 ℃ -90 ℃) and the time length of exchange (0.25 h-48 h). Following the exchange step, by letting the films sit in DMF solvent, the films were thoroughly washed to remove any hovering counter ions (eg: Cl^-) or Rh precursor that is not exchanged and could be trapped in the pores of the MOF film. DMF was used for most of the washing steps since it has been identified as a superior washing solvent that got rid of more Cl^- in a given time compared to ethanol. During the washing step, the solvent was replaced with a fresh batch every 30 min for the first two hours, in order to quickly remove the unwanted components from the surroundings and make the wash more efficient. Additionally, Rh acetate precursor was also used in the dip coating step along with Cu acetate and H_3BTC in order to synthesize bimetallic film using a different procedure where the synthesis and transmetallation steps were combined.

Characterization

Grazing incidence wide angle X-ray scattering (GIWAXS) data was collected using a Xenocs GeniX3D microfocus source with a Cu target and a Hybrid Pixel Array Pilatus detector (Dectris) was used for collecting scattering patterns on a SAXSLab Ganesha at the South Carolina SAXS Collaborative, to determine the crystallinity of the MOF films pre and post transmetallation. GIWAXS measurements were collected over the diffraction angle (2θ) of 0-42°, on the MOF films grown on Al_2O_3 coated Si wafers at an incident angle of 4˚ at room temperature for 30 minutes. GIWAXS spectra was collected pre and post transmetallation to investigate Rh incorporation into the CuBTC framework.

The elemental composition of the MOF films was determined using XPS with a Kratos AXIS Ultra DLD system including a monochromatic Al K_α source, hemispherical analyzer and a charge neutralizer[3,24] which were installed in a UHV chamber with a base pressure of $1x10^{-9}$ torr and a load lock chamber for swift sample introduction without breaking vacuum. The C(1s) and O(1s) regions were collected with a dwell time of 800 ms each, while Cu(2p) and Rh(3d) regions were collected using a dwell time of 1000 ms each. Cu(LMM), Cl(2p), Al(2s), Si(2p), valence band and N(1s) regions were collected with a dwell time of 600 ms each. The energy step size for all the regions mentioned above were 0.06 eV, with a pass energy of 40 eV. A rough survey scan was performed with a dwell time of 300 ms, pass energy of 160 eV and a step size of 0.8 eV to confirm that there was no contamination that took place during the sample preparation step. Due to the insulating nature of MOF samples, a charge neutralizer was used to shoot low energy electrons at the sample to compensate for sample charging from photoelectron emission. The adventitious C(1s) peak was set to 284.8 eV to be used as an internal reference to determine the binding energies for the rest of the regions collected. To determine the Rh: Cl ratio, Kratos atomic sensitivity factors 4.822 and 0.891 were used for the Rh(3d) and Cl(2p) region respectively.

Atomic force microscopy (AFM) images were collected on the films before and after the transmetallation step, in the tapping mode, in air, using a Multimode Nanoscope IIIA system (Digital Instruments Inc.) with commercial Si cantilevers (ACT, Applied NanoStructures) at a scan rate of 1 Hz to study the topography of the MOF films.

4.3 RESULTS AND DISCUSSION

The GIWAXS spectrum revealed that the sequential dip coating method enabled the growth of crystalline thin CuBTC films with the predicted paddle wheel structure. The

simulated CuBTC GIWAXS spectra with different crystalline phase assignments was very similar to that obtained for the films synthesized via the dip coating method, as illustrated in Figure 4.5 traces (a) and (c).This is also in agreement with the structure reported in the literature.[10,12,17,24,37,38] Previous work by the Chen group in collaboration with the Shustova group demonstrated that bimetallic CuRhBTC powder synthesized from Rh exchange of CuBTC has Rh^{2+} incorporated in the paddle wheel structure with some of the Cu in the framework being replaced with the second metal Rh.[19] Similarly, post transmetallation GIWAXS spectra was collected for the MOF thin films in order to investigate the preservation of the crystal structure and the incorporation of Rh into the paddle wheel structure via Cu node replacement. Post Rh exchange with $RhCl_3$ precursor, the paddle wheel structure was retained as depicted in Figure 4.5, trace (d). Trace (e) shows that the film synthesized by using Rh acetate in the dip coating step also showed a similar GIWAXS spectra to a typical CuBTC film indicating that there was an isostructural, crystalline film formed.

XPS revealed the presence of copper, carbon and oxygen in the monometallic film, verifying that the paddle wheel structure had Cu in the binuclear nodes and BTC ligands bound to it. The XPS data was also consistent with that of the powder CuBTC MOF reported in prior work.[19] The C(1s) region had two peaks indicating that there were two types of carbon detected in the films. The lower binding energy C(1s) peak which was used as the internal standard was set to 284.8 eV and this peak has a major contribution from adventitious carbon and a smaller contribution from aliphatic carbons.[39,40] The additional peak in the C(1s) region that is observed to have a binding energy of 288.8 eV is attributed to the presence of C=O groups coming from the MOF ligands.[39,40] The ratio between the

two C(1s) peaks gives us an idea of the thickness of the film and can also be used to evaluate the extent of film delamination post transmetallation and solvent wash compared to the initial monometallic CuBTC film.[30] Traces (a)-(f) in Figure 4.6 illustrate the C(1s) regions for four CuBTC films subject to Rh precursor treatment (the treatment parameters are listed in Table 4.1), one CuBTC film and a blank Al_2O_3 substrate from top to bottom. The Al(2s) and Si(2p) regions can also be used to estimate the film thickness because the signal for these regions will give us an idea about the amount of exposed substrate. The 284.8 eV C(1s) peak heights for all the films in Figure 4.6 have been scaled to match that of CuBTC to enable visual comparison of the 284.8 eV to 288.8 eV peak ratio which dictates the film thickness. It can be observed that the C(1s) peak at 288.8 eV is much smaller for the CuRhBTC film trace (d) which was subject to an extended 48 hour wash in DMF solvent, indicating the presence of a thinner layer of film compared to (a) which was only washed for 24 hours. The XPS C(1s) spectra for the blank Al_2O_3 substrate also had a large peak at 248.8 eV as illustrated in trace (f), verifying that the peak has a major contribution from adventitious carbon. The blank substrate also appeared to have a much smaller peak at 288.8 eV, even though no film was grown on it. This can be attributed to the C=O from atmospheric CO_2, which has been reported to adsorb on Al_2O_3.[41–43]

The oxidation states of the Rh species were determined by collecting XPS on two standard Rh compounds: $RhCl_3$ and $Rh_2(CH_3COO^-)_4$ which are known to have 3+ and 2+ oxidation states respectively as illustrated in Figure 4.7. The XPS data collected on a specific sample is given a fixed color in all the different regions for the sake of cross comparison. Comparing the Rh(3d) and Cl(2p) regions for the $RhCl_3$ exchanged film, which is brown in color in Figures 4.8 & 4.9, it can be observed that both Rh^{3+} and Cl^-

were present after the Rh precursor treatment in the film that was not washed for an extended time. In order to confirm that the Rh was incorporated in the framework and was not filling the pores of the MOF film in the form of $RhCl_3$, longer DMF washes were conducted. After a 48 hour wash the Cl(2p) signal was comparable with that of a Rh acetate dip coated film which had no source of Cl as observed by comparing traces (c) & (d) in Figure 4.9. However, the Rh(3d) signal which significantly diminished was still undeniably present as observed by comparing traces (b) & (e) in Figure 4.8. Hence, the longer DMF wash appeared to have removed the excess $RhCl_3$ and left behind the exchanged Rh in the framework. Regardless of the Rh oxidation state in the initial Rh precursor being 3+ ($RhCl_3$) or 2+ (Rh acetate), the MOF films that were subject to the transmetallation treatment predominantly had Rh^{3+} ions identified by the 310.1 eV [19,44] binding energy from XPS studies. This is different to what was previously reported with the well characterized bimetallic CuRhBTC MOF powder where Rh^{2+} (309.2 eV) was the predominant species as observed in Figure 4.8, trace (a).[19] However, XPS also revealed that the bimetallic MOF film subject to a 48 hour DMF wash (trace (e) in Figure 4.8) showed the most evidence for the presence of a mixture of both Rh 3+ and 2+ species. See Figure 4.10 for deconvoluted peak spectra showing Rh^{3+} and Rh^{2+} oxidation states. It is also true that this particular film had very few layers of film remaining after the extended wash step, which was evident from the lower C(1s) signal at 288.8 eV.

Cu^{2+} is the predominant Cu species observed in the films and is attributed to the Cu($2p_{3/2}$) peak at 935.0 eV [8,24,40] depicted in Figure 4.11. A shoulder for Cu^{+} observed [31] at 933.4 eV [24] was also present in some of the MOF films (eg: traces (a) and (c) in Figure 4.11). The presence of Cu in the +1 oxidation state is attributed to the reduction of the Cu^{2+}

under vacuum or from being irradiated with X-rays.[24] Satellite features characteristic of Cu^{2+} were present at 940.0 eV and 944.5 eV, further verifying that it was the predominant Cu species.[8,20,24] The film that had a mixture of 3+ and 2+ Rh oxidation states also contained very little Cu as observed in Figure 4.11, trace (d). One reason for this observation could be the fewer layers of MOF film present in this sample from the loss of film with the 48 hour extended washing step. Another reason could be that this film sustained a large amount of Rh exchange from the extended 33 hour transmetallation step in $RhCl_3$. Hence, the observed reduction in the Cu(2p) peak can be explained by a combined effect that is a result of the above-mentioned causes. XPS can also be used to quantify the Rh:Cu ratio in the framework. However, extended washes for over 48 hours are required to first remove all non-exchanged Rh precursor molecules that can get into the MOF pores.

The binding energy of the O(1s) peak in the CuBTC film was observed to be 532.0 eV [8] which is attributed to the oxygen in the Cu-O-C bond that forms between the Cu metal node and the BTC ligand.[8,20,40] Post transmetallation in $RhCl_3$ or Rh acetate, the O(1s) peak broadened in the higher binding energy region compared to the monometallic CuBTC for the films treated in Rh precursor solutions as observed in Figure 4.12. For most of the films subjected to the Rh precursor exchange treatment, a broad oxygen region was observed even when they seemed to have predominantly unexchanged $RhCl_3$, which was evident from the larger Cl(2p) signals. This broadening towards the higher binding energies was also observed with the previously studied powder CuRhBTC MOFs compared to its monometallic CuBTC counterpart as illustrated in Figure 4.15 included in the supplement information section. In Figure 4.15, where the O(1s) region of Rh acetate is plotted with

that of the powder MOFs, it can be observed that neither CuBTC with equivalent Cu^{2+}-O bonds nor Rh acetate with equivalent Rh^{2+}-O bonds have an O(1s) peak at higher binding energies, near 534.5 eV. This is also true for Rh^{3+}-O bonds which have been reported for Rh_2O_3[45,46]. However, oxygens with binding energy > 532 eV have been reported for Rh compounds that have less electron rich oxygens such as O_2, OH or H_2O adsorbed on the surface.[47–50] It is also worth noting that the powder MOFs have been treated at ~160 ℃ for 24-48 hours under vacuum before the XPS analysis, to remove any water and solvent ligands present. Hence, the O(1s) peak broadening didn't appear to directly correlate with the extent of Rh exchanged in the framework. All traces in Figure 4.12 and Figure 4.15 have been scaled to match the height of the CuBTC O(1s) peak to compare the peak broadening effectively. As observed in Figure 4.12, the O(1s) region of the Al_2O_3-Si substrate itself has a peak with a binding energy of 531.4 eV.[51,52,56] Therefore, the broadening of the 534.5 eV peak at higher binding energy should not be due to substrate exposure from film washing off either. The film made via sequential dip coating in Cu acetate, H_3BTC ligand and Rh acetate solutions had an O(1s) region that was similar to the CuBTC films in that it was narrow and had a binding energy of 532.0 eV as observed in Figure 4.12. This suggests that the crystalline film present is more similar to CuBTC itself with oxidized Rh^{3+} present in the pores. This experiment also provides evidence to suggest that the mere presence of Rh^{3+} in the pores does not cause the O(1s) region to broaden.

The topography of the monometallic and bimetallic MOF films was analyzed using AFM in the tapping mode. In order to grow films throughout the substrate, 40 cycles of sequential dip coating was used as it has been observed from previous studies that 40 cycles was sufficient to cover the substrate completely.[30] Figure 4.13 illustrate the CuBTC film

had octahedral crystallites [9,40,53] that were on average 80-130 nm in height and 120-300 nm wide with a root mean squared (RMS) roughness of ~28 nm. AFM images of a film that was exchanged in 0.0386 M $RhCl_3$ in DMF for 22 hours at room temperature and washed for 9.5 hours in DMF had crystallites that were 90-110 in height and 200-250 nm wide indicating a slight reduction in the crystallite sizes. The crystallite shapes in the films that were subject to Rh precursor treatment were more round than octahedral after extensive soaking in solvent during the exchange and wash steps as observed in Figure 4.14. This could be due to the exchanged film having less well-defined crystal facets.

4.4 CONCLUSION

Bimetallic BTC based MOFs have interesting applications in heterogeneous catalysis and electronics among others. However, the powder MOFs can be complicated to study due to their three-dimensional network nature. By synthesizing thin film of these MOFs to reduce the extension of the framework in one-dimension, analogous 2D surfaces that are more suitable for fundamental studies and thin film applications can be synthesized. Thin films of monometallic CuBTC were successfully grown on a Si substrate coated with Al_2O_3 in a layer by layer fashion via a dip coating method and characterized with GIWAXS, AFM and XPS to verify the formation of thin films with the well-known crystalline MOF network. GIWAXS and XPS data collected post transmetallation with $RhCl_3$ precursor suggest that isostructural bimetallic films with node Cu^{2+} replacement by Rh can be synthesized. However, extended DMF washes are required to remove all non-exchanged precursor molecules from the pores of the MOF. The absence of Cl with persisting Rh was observed with multiple bimetallic films subject to extended washes further indicating that the Rh had exchanged in to the CuBTC framework.

Table 4.1: Parameters used for the MOF film Rh exchanges. All exchanges were conducted at room temperature with precursor solutions made in ethanol solvent

Film label	**trace color**	**Rh precursor used for exchange**	**Exchange precursor concentration (mM)**	**Exchange time length (h)**	**Wash time length in DMF (h)**
$RhCl_3$ Exchanged	brown	$RhCl_3$	1	4.5	24
Rh acetate exchanged	light blue	Rh acetate	1	6	3.5
Rh acetate dip coated	green	Rh acetate	1	used Rh acetate in the dip coating step	
$RhCl_3$ Exchanged extended wash	purple	$RhCl_3$	3	33	48

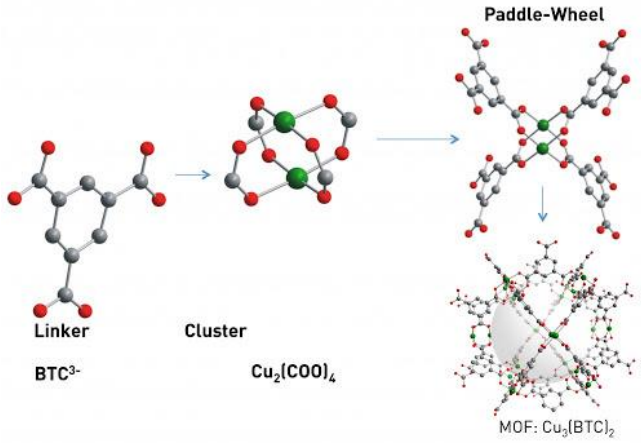

Figure 4.1: CuBTC synthesis and structure [55]

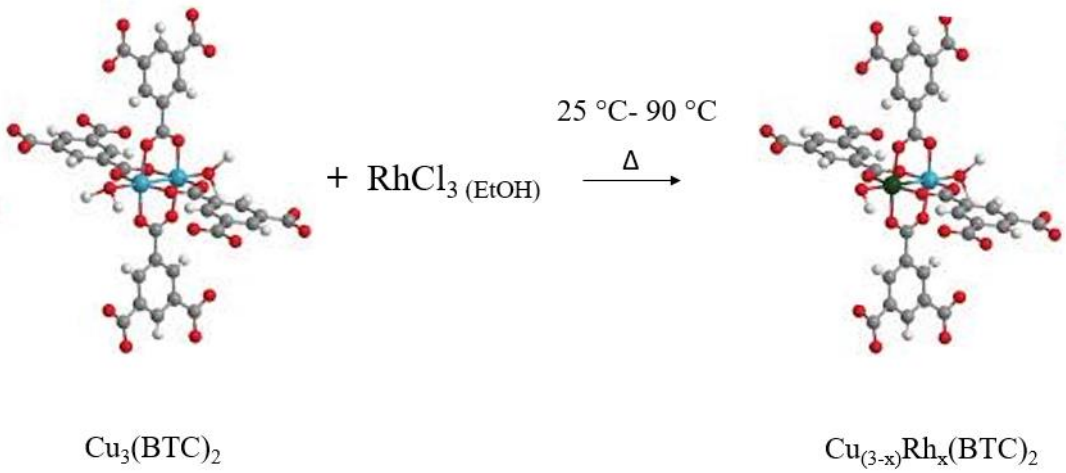

Figure 4.2: Second metal incorporation via node metal exchange[54]

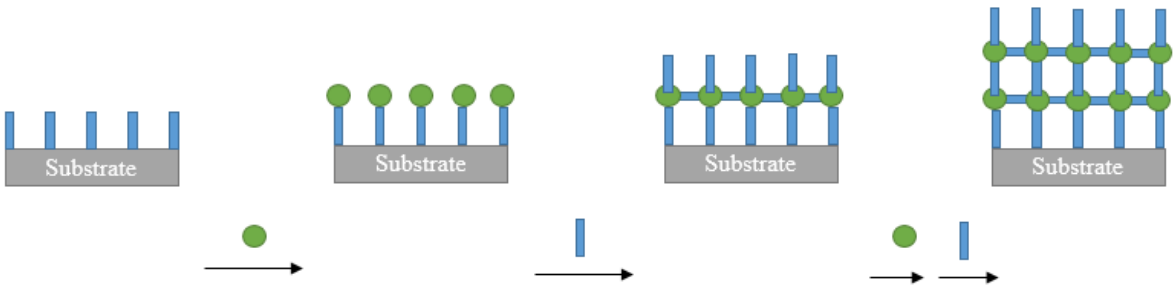

Figure 4.3: Layer-by-layer growth of thin MOF films

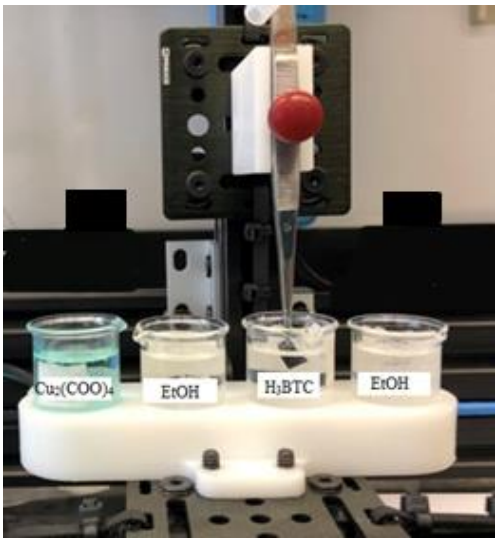

Figure 4.4: Home-made automated dip coater used to soak the substrate in Cu acetate and H_3BTC solutions with ethanol rinsing and N_2 drying steps in between to synthesize thin films of CuBTC

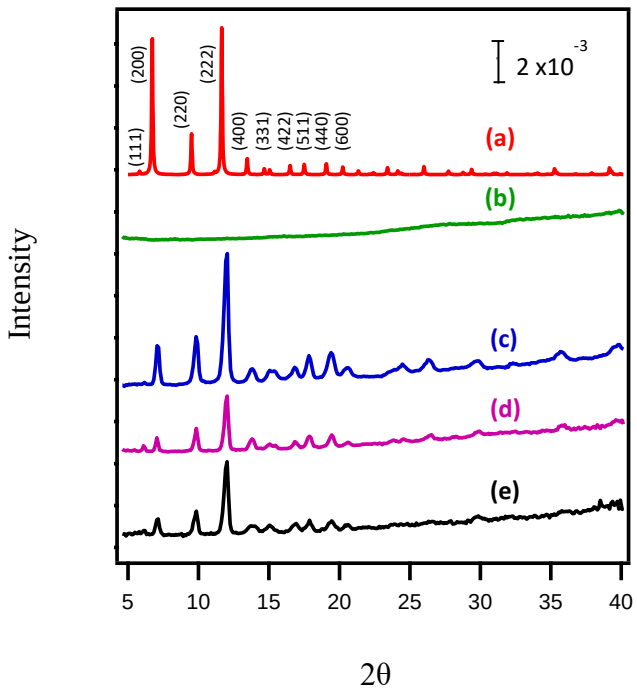

Figure 4.5: GIWAXS spectra for simulated CuBTC (a); Al_2O_3 -Si substrate (b); CuBTC thin film (c); $RhCl_3$ exchnaged CuBTC film (d); Rh acetate dip coated film(e)

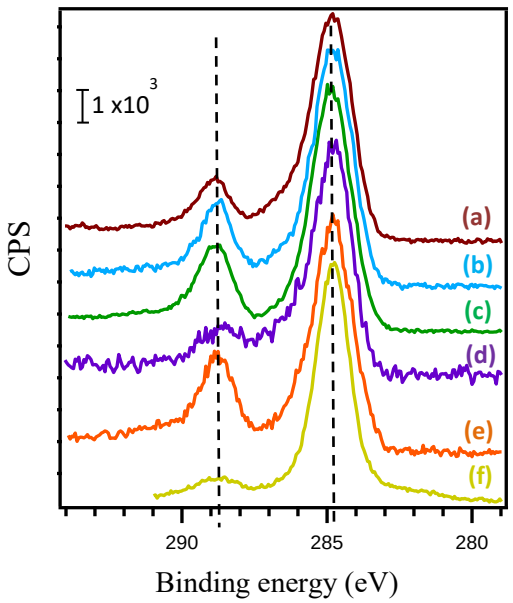

Figure 4.6: XPS C(1s) spectra for films; $RhCl_3$ exchanged CuBTC (a); Rh acetate exchanged CuBTC (b); Rh acetate dip coated (c); $RhCl_3$ exchanged CuBTC with extended wash (d); CuBTC (e); Al_2O_3 -Si substrate (f)

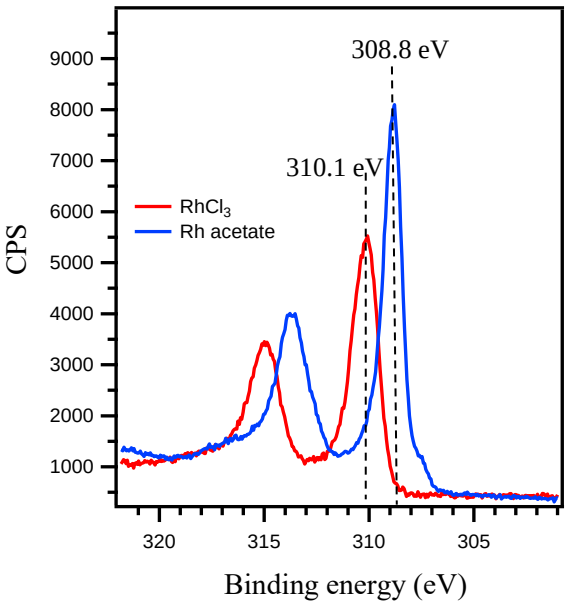

Figure 4.7: Rh(3d) XPS region for as received Rh(III) chloride-red and Rh(II) acetate-blue standards also used as precursors for the Rh transmetallation

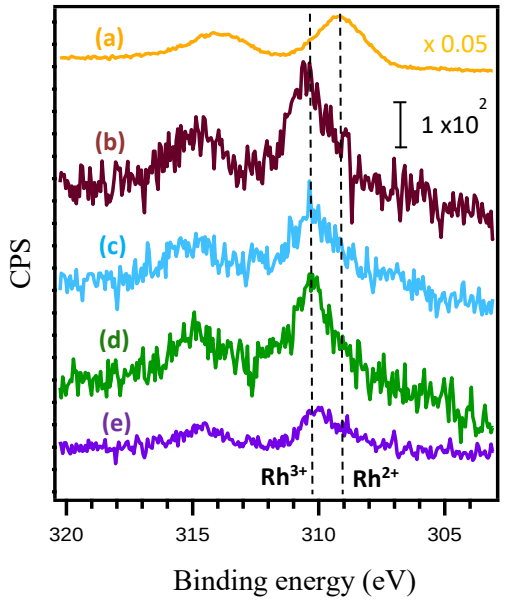

Figure 4.8: Rh(3d) XPS region for powder CuRhBTC MOF (a); $RhCl_3$ exchanged CuBTC film (b); Rh acetate exchanged CuBTC film(c); Rh acetate dip coated film(d); $RhCl_3$ exchanged film with extended wash (e)

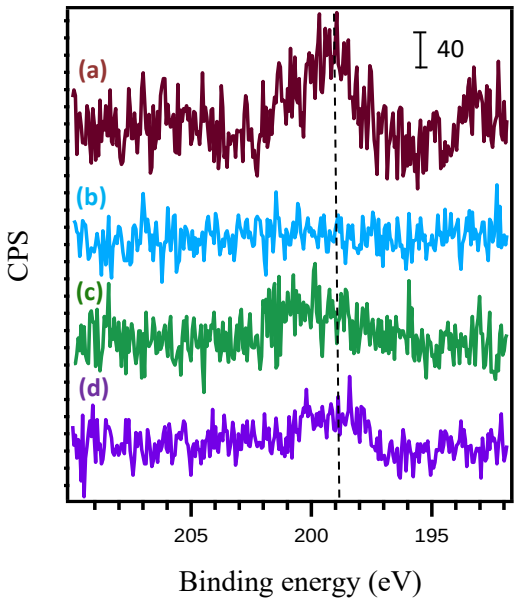

Figure 4.9: Cl(2p) XPS reigion for films; $RhCl_3$ exchanged CuBTC (a); Rh acetate exchanged CuBTC (b); Rh acetate dip coated (c); $RhCl_3$ exchanged with extended wash (d)

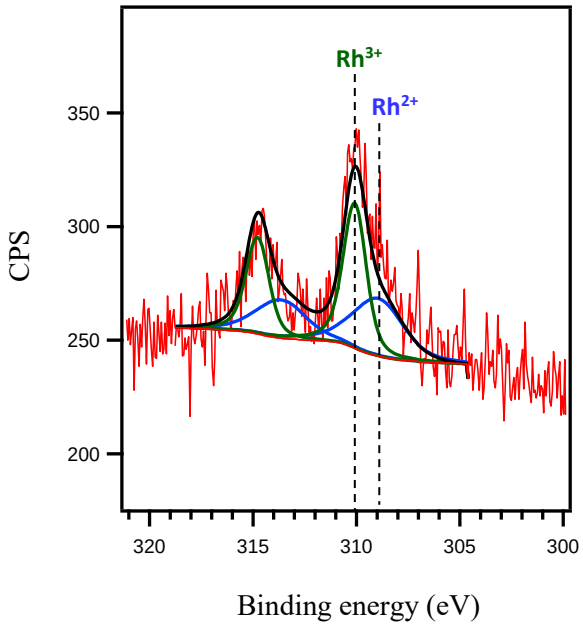

Figure 4.10: Fitted Rh(3d) region for $RhCl_3$ exchanged film with extended wash showing the presence of Rh^{3+} and Rh^{2+} species

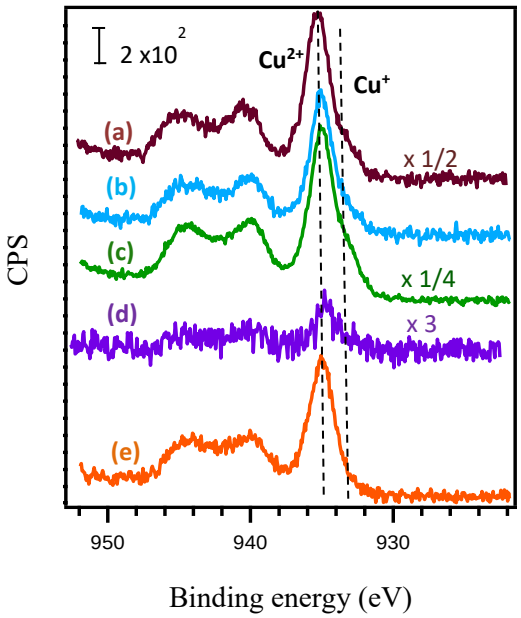

Figure 4.11: Cu(2p) XPS region for films; $RhCl_3$ exchanged CuBTC (a); Rh acetate exchanged CuBTC (b); Rh acetate dip coated(c); $RhCl_3$ exchanged with extended wash (d); CuBTC(e)

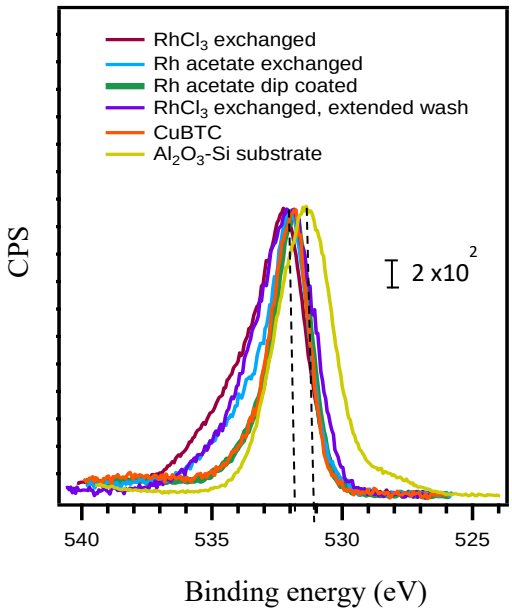

Figure 4.12: O(1s) XPS region for Al_2O_3 -Si substrate, CuBTC and Rh exchanged CuBTC films

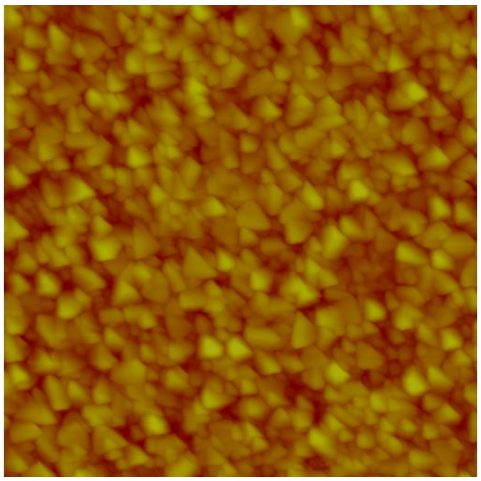

Figure 4.13: CuBTC film grown from 40 cycles of dip coating. 5μm x 5μm

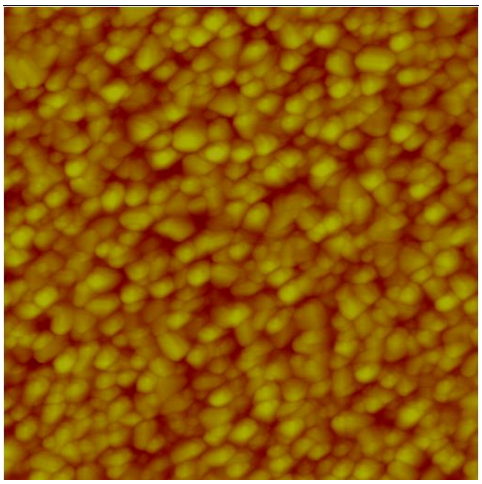

Figure 4.14: $RhCl_3$ exchanged CuBTC film. 5μm x 5μm

4.5 SUPPLEMENT INFORMATION SECTION

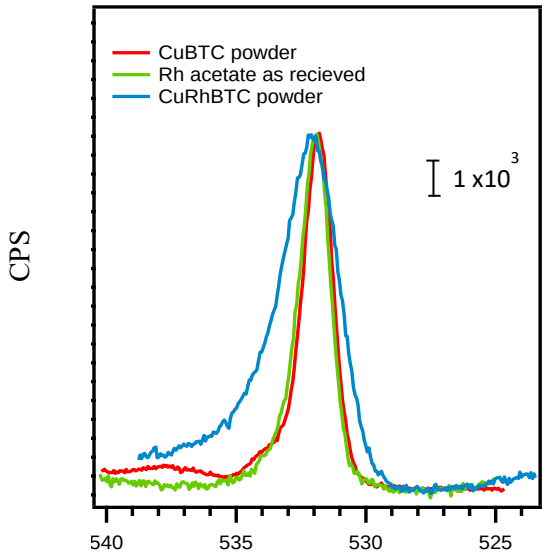

Figure 4.15: O(1s) XPS region for powder CuBTC and CuRhBTC MOFs plotted with that of as received Rh acetate

4.6 ACKNOWLEDGEMENTS

I would like to express my sincere gratitude to the ASPIRE grant and the department of energy for funding this project work. Additional thanks go to Dr. Amy Brandt for GIWAXS data collection, Deependra Shakya for AFM image collection, Dr. Gift Metavarayuth for her assistance with film growth and exchange, Dr. Karakalos Stavros for collecting XPS on the MOF films and the Shustova group for their extremely helpful insights.

4.7 REFERENCES

1. Yuan S, Feng L, Wang K, et al. Stable Metal–Organic Frameworks: Design, Synthesis, and Applications. *Adv Mater*. 2018;30(37):1-35. doi:10.1002/adma.201704303
2. Fleker O, Borenstein A, Lavi R, Benisvy L, Ruthstein S, Aurbach D. Preparation and Properties of Metal Organic Framework/Activated Carbon Composite Materials. *Langmuir*. 2016;32(19):4935-4944. doi:10.1021/acs.langmuir.6b00528
3. Dolgopolova EA, Brandt AJ, Ejegbavwo OA, et al. Electronic Properties of Bimetallic Metal-Organic Frameworks (MOFs): Tailoring the Density of Electronic States through MOF Modularity. *J Am Chem Soc*. 2017;139(14):5201-5209. doi:10.1021/jacs.7b01125
4. Duke AS, Dolgopolova EA, Galhenage RP, et al. Active Sites in Copper-Based Metal-Organic Frameworks: Understanding Substrate Dynamics, Redox Processes, and Valence-Band Structure. *J Phys Chem C*. 2015;119(49):27457-27466. doi:10.1021/acs.jpcc.5b08053
5. Safaei M, Foroughi MM, Ebrahimpoor N, Jahani S, Omidi A, Khatami M. A review on metal-organic frameworks: Synthesis and applications. *TrAC - Trends Anal Chem*. 2019;118:401-425. doi:10.1016/j.trac.2019.06.007
6. Wang C, Liu D, Lin W. Metal-organic frameworks as a tunable platform for designing functional molecular materials. *J Am Chem Soc*. 2013;135(36):13222-13234. doi:10.1021/ja308229p
7. Furtado AMB, Liu J, Wang Y, Levan MD. Mesoporous silica-metal organic composite: Synthesis, characterization, and ammonia adsorption. *J Mater Chem*. 2011;21(18):6698-6706. doi:10.1039/c1jm10451a
8. Liu J, Li XM, He J, Wang LY, Lei J Du. Combining the photocatalysis and absorption properties of core-shell Cu-BTC@TiO2 microspheres: Highly efficient desulfurization of thiophenic compounds from fuel. *Materials (Basel)*. 2018;11(11). doi:10.3390/ma11112209

9. Qu ZG, Wang H, Zhang W. Highly efficient adsorbent design using a Cu-BTC/CuO/carbon fiber paper composite for high CH4/N2 selectivity. *RSC Adv*. 2017;7(23):14206-14218. doi:10.1039/c6ra28124a
10. Peng MM, Kim DK, Aziz A, Back KR, Jeon UJ, Jang HT. CO2 adsorption of metal organic framework material Cu-BTC via different preparation routes. *Commun Comput Inf Sci*. 2012;341 CCIS:244-251. doi:10.1007/978-3-642-35248-5-34
11. Bian Y, Wang R, Wang S, et al. Metal-organic framework-based nanofiber filters for effective indoor air quality control. *J Mater Chem A*. 2018;6(32):15807-15814. doi:10.1039/c8ta04539a
12. Zhang W, Meng S, Wang H, He Y. Metal organic frameworks enhanced graphene oxide electrode for humidity sensor. *J Phys Conf Ser*. 2018;986(1). doi:10.1088/1742-6596/986/1/012013
13. Yin W, Tao CA, Zou X, Wang F, Qu T, Wang J. The tuning of optical properties of nanoscale MOFs-based thin film through post-modification. *Nanomaterials*. 2017;7(9). doi:10.3390/nano7090242
14. Ji L, Hao J, Wu K, Yang N. Potential-Tunable Metal-Organic Frameworks: Electrosynthesis, Properties, and Applications for Sensing of Organic Molecules. *J Phys Chem C*. 2019;123(4):2248-2255. doi:10.1021/acs.jpcc.8b10448
15. Yilmaz G, Peh SB, Zhao D, Ho GW. Atomic- and Molecular-Level Design of Functional Metal–Organic Frameworks (MOFs) and Derivatives for Energy and Environmental Applications. *Adv Sci*. 2019;6(21). doi:10.1002/advs.201901129
16. So MC, Jin S, Son HJ, Wiederrecht GP, Farha OK, Hupp JT. Layer-by-layer fabrication of oriented porous thin films based on porphyrin-containing metal-organic frameworks. *J Am Chem Soc*. 2013;135(42):15698-15701. doi:10.1021/ja4078705
17. Zhang X, Zhan Z, Li Z, Di L. Thermal activation of CuBTC MOF for CO Oxidation: The effect of activation atmosphere. *Catalysts*. 2017;7(4). doi:10.3390/catal7040106
18. Neufeld MJ, Harding JL, Reynolds MM. Immobilization of Metal–Organic Framework Copper(II) Benzene-1,3,5-tricarboxylate (CuBTC) onto Cotton Fabric as a Nitric Oxide Release Catalyst. *ACS Appl Mater Interfaces*. 2015;7(48):26742-26750. doi:10.1021/acsami.5b08773
19. Shakya DM, Ejegbavwo OA, Rajeshkumar T, et al. Selective Catalytic Chemistry at Rhodium(II) Nodes in Bimetallic Metal–Organic Frameworks. *Angew Chemie - Int Ed*. 2019;58(46):16533-16537. doi:10.1002/anie.201908761
20. Senthil Kumar R, Senthil Kumar S, Anbu Kulandainathan M. Efficient electrosynthesis of highly active Cu3(BTC) 2-MOF and its catalytic application to chemical reduction. *Microporous Mesoporous Mater*. 2013;168:57-64. doi:10.1016/j.micromeso.2012.09.028
21. Santiago Portillo A, Baldoví HG, García Fernandez MT, et al. Ti as Mediator in the Photoinduced Electron Transfer of Mixed-Metal NH2-UiO-66(Zr/Ti): Transient Absorption Spectroscopy Study and Application in Photovoltaic Cell. *J Phys Chem C*. 2017;121(12):7015-7024. doi:10.1021/acs.jpcc.6b13068

22. Syzgantseva MA, Ireland CP, Ebrahim FM, Smit B, Syzgantseva OA. Metal Substitution as the Method of Modifying Electronic Structure of Metal-Organic Frameworks. *J Am Chem Soc*. 2019;141(15):6271-6278. doi:10.1021/jacs.8b13667
23. Xie LS, Sun L, Wan R, et al. Tunable Mixed-Valence Doping toward Record Electrical Conductivity in a Three-Dimensional Metal-Organic Framework. *J Am Chem Soc*. 2018;140(24):7411-7414. doi:10.1021/jacs.8b03604
24. Duke AS, Dolgopolova EA, Galhenage RP, et al. Active Sites in Copper-Based Metal-Organic Frameworks: Understanding Substrate Dynamics, Redox Processes, and Valence-Band Structure. *J Phys Chem C*. 2015;119(49):27457-27466. doi:10.1021/acs.jpcc.5b08053
25. Baumann AE, Aversa GE, Roy A, Falk ML, Bedford NM, Thoi VS. Promoting sulfur adsorption using surface Cu sites in metal-organic frameworks for lithium sulfur batteries. *J Mater Chem A*. 2018;6(11):4811-4821. doi:10.1039/c8ta01057a
26. Cai Y, Kulkarni AR, Huang YG, Sholl DS, Walton KS. Control of metal-organic framework crystal topology by ligand functionalization: Functionalized HKUST-1 derivatives. *Cryst Growth Des*. 2014;14(11):6122-6128. doi:10.1021/cg501285q
27. Decoste JB, Peterson GW, Schindler BJ, Killops KL, Browe MA, Mahle JJ. The effect of water adsorption on the structure of the carboxylate containing metal-organic frameworks Cu-BTC, Mg-MOF-74, and UiO-66. *J Mater Chem A*. 2013;1(38):11922-11932. doi:10.1039/c3ta12497e
28. Hall JN, Bollini P. Structure, characterization, and catalytic properties of open-metal sites in metal organic frameworks. *React Chem Eng*. 2019;4(2):207-222. doi:10.1039/c8re00228b
29. Grajciar L, Bludský O, Nachtigall P. Water adsorption on coordinatively unsaturated sites in CuBTC MOF. *J Phys Chem Lett*. 2010;1(23):3354-3359. doi:10.1021/jz101378z
30. Brandt, A. J; Shakya D.M; Metavarayuth, K; Dolgopolova, E; Hensley, L; Duke, A.S; Farzandh, S; Shustova N. and DCA. Growth of Crystalline, Bimetallic Metal Organic Framework Films via Dip-Coating and Transmetallation. Manuscript in preparation
31. Shekhah O, Liu J, Fischer RA, Wöll C. MOF thin films: Existing and future applications. *Chem Soc Rev*. 2011;40(2):1081-1106. doi:10.1039/c0cs00147c
32. Wang Z, Wöll C. Fabrication of Metal–Organic Framework Thin Films Using Programmed Layer-by-Layer Assembly Techniques. *Adv Mater Technol*. 2019;4(5):1800413. doi:10.1002/admt.201800413
33. Bétard A, Fischer RA. Metal-organic framework thin films: From fundamentals to applications. *Chem Rev*. 2012;112(2):1055-1083. doi:10.1021/cr200167v
34. Shekhah O. Layer-by-layer method for the synthesis and growth of surface mounted metal-organic frameworks (SURMOFS). *Materials (Basel)*. 2010;3(2):1302-1315. doi:10.3390/ma3021302
35. Zacher D, Yusenko K, Bétard A, et al. Liquid-phase epitaxy of multicomponent layer-based porous coordination polymer thin films of [M(L)(P)0.5] type: Importance of deposition sequence on the oriented growth. *Chem - A Eur J*. 2011;17(5):1448-1455. doi:10.1002/chem.201002381

36. Ikigaki K, Okada K, Tokudome Y, et al. MOF-on-MOF: Oriented Growth of Multiple Layered Thin Films of Metal–Organic Frameworks. *Angew Chemie - Int Ed*. 2019;58(21):6886-6890. doi:10.1002/anie.201901707
37. Duan C, Li F, Zhang H, Li J, Wang X, Xi H. Template synthesis of hierarchical porous metal-organic frameworks with tunable porosity. *RSC Adv*. 2017;7(82):52245-52251. doi:10.1039/c7ra08798e
38. Abbasi AR, Rizvandi M. Influence of the ultrasound-assisted synthesis of Cu–BTC metal–organic frameworks nanoparticles on uptake and release properties of rifampicin. *Ultrason Sonochem*. 2018;40:465-471. doi:10.1016/j.ultsonch.2017.07.041
39. Furtado AMB, Liu J, Wang Y, Levan MD. Mesoporous silica-metal organic composite: Synthesis, characterization, and ammonia adsorption. *J Mater Chem*. 2011;21(18):6698-6706. doi:10.1039/c1jm10451a
40. Li X, Liu H, Jia X, Li G, An T, Gao Y. Novel approach for removing brominated flame retardant from aquatic environments using Cu/Fe-based metal-organic frameworks: A case of hexabromocyclododecane (HBCD). *Sci Total Environ*. 2018;621:1533-1541. doi:10.1016/j.scitotenv.2017.10.075
41. Li G, Xiao P, Webley P. Binary Adsorption Equilibrium of Carbon Dioxide and Water Vapor on Activated Alumina. *Langmuir*. 2009;25(18):10666-10675. doi:10.1021/la901107s
42. Pan Y xiang, Liu C jun, Wiltowski TS, Ge Q. CO2 adsorption and activation over γ-Al2O3-supported transition metal dimers: A density functional study. *Catal Today*. 2009;147(2):68-76. doi:10.1016/j.cattod.2009.05.005
43. Ornelas-Lizcano JC, Guirado-López RA. Adsorption of carbon monoxide on small aluminum oxide clusters: Role of the local atomic environment and charge state on the oxidation of the CO molecule. *J Chem Phys*. 2015;142(12):124311. doi:10.1063/1.4916320
44. Zou R, Wen S, Zhang L, Liu L, Yue D. Preparation of Rh-SiO2 fiber catalyst with superior activity and reusability by electrospinning. *RSC Adv*. 2015;5(121):99884-99891. doi:10.1039/c5ra20473a
45. Moreno FernÃ¡ndez H, Zangrando M, Sauthier G, GoÃ±i AR, Carlino V, Pellegrin E. Towards chemically neutral carbon cleaning processes: plasma cleaning of Ni, Rh and Al reflective optical coatings and thin Al filters for free-electron lasers and synchrotron beamline applications. *J Synchrotron Radiat*. 2018;25(6):1642-1649. doi:10.1107/S1600577518014017
46. Blomberg S, Lundgren E, Westerström R, et al. Structure of the Rh2O3(0001) surface. *Surf Sci*. 2012;606(17-18):1416-1421. doi:10.1016/j.susc.2012.05.004
47. A.A Tolia, R.J. Smiley, W.N deglass et al. Surface Oxidation of Rhodium at Ambient Pressure as Probed by Surace-Enhanced Raman and X-ray Photoelectron Spectroscopies. *J catal*. 1994;150:56-70.
48. Abe Y, Kato K, Kawamura M, Sasaki K. Electrical properties of amorphous Rh oxide thin films prepared by reactive sputtering. *Japanese J Appl Physics, Part 1 Regul Pap Short Notes Rev Pap*. 2000;39(1):245-247. doi:10.1143/JJAP.39.245
49. Kibis LS, Stadnichenko AI, Koscheev S V., Zaikovskii VI, Boronin AI. XPS Study of Nanostructured Rhodium Oxide Film Comprising Rh4+ Species. *J Phys Chem C*. 2016;120(34):19142-19150. doi:10.1021/acs.jpcc.6b05219

50. Marot L, Mathys D, Temmerman G De, Oelhafen P. Characterization of sub-stoichiometric rhodium oxide deposited by magnetron sputtering. *Surf Sci*. 2008;602(21):3375-3380. doi:10.1016/j.susc.2008.09.012
51. Strohmeier BR. Gamma-Alumina (γ-Al 2 O 3) by XPS . *Surf Sci Spectra*. 1994;3(2):135-140. doi:10.1116/1.1247774
52. Fu Q, Wagner T, Rühle M. Hydroxylated α-Al2O3 (0 0 0 1) surfaces and metal/α-Al2O3 (0 0 0 1) interfaces. *Surf Sci*. 2006;600(21):4870-4877. doi:10.1016/j.susc.2006.08.008
53. Doan H V., Fang Y, Yao B, et al. Controlled Formation of Hierarchical Metal-Organic Frameworks Using CO2-Expanded Solvent Systems. *ACS Sustain Chem Eng*. 2017;5(9):7887-7893. doi:10.1021/acssuschemeng.7b01429
54. Kaaskel S. Metal-organic frameworks: record-breakers in porosity - labor&more. http://www.int.laborundmore.com/archive/620180/Metal-organic-frameworks%3A-record-breakers-in-porosity.html. Published April 2015. Accessed February 17, 2020.
55. Gotthardt MA, Schoch R, Wolf S, Bauer M, Kleist W. Synthesis and characterization of bimetallic metal-organic framework Cu-Ru-BTC with HKUST-1 structure. *Dalt Trans*. 2015;44(5):2052-2056. doi:10.1039/c4dt02491e
56. J. Moulder, W.F. Stickle, P.E. Sobol, K.D. Bomben, The Handbook of the X-ray Photoelectron Spectroscopy, Pekin-Elmer Corporation, 1992.